Chapter 7
Creating Nanostructures with Lasers

Paolo M. Ossi and Maria Dinescu

Abstract Lasers represent an efficient and versatile tool to produce and to arrange in organized dispositions nanometer-sized particles, obtaining extended nanostructures with increasing degrees of complexity. In the first part of the chapter, the basic mechanisms of nanoparticle formation for nanosecond laser ablation in an ambient gas atmosphere and femtosecond ablation in vacuum are considered. In the former case, atomic or molecular clusters grow during the propagation through the ambient gas of the plasma plume resulting from target irradiation. Plume expansion is affected by laser wavelength and fluence, nature and pressure of the background gas, target to substrate distance. Cluster size and kinetic energy, together with the related distributions at landing onto the substrate depend on plasma dynamics and determine relevant differences of morphology and nanostructure of the growing film. Popular models for the propagation of an ablation plume through a gas at increasing pressure are recalled before deducing the average asymptotic size of particles nucleated in the plume, to be compared with available data from selected experiments. The synthesis of spatially uniform distributions of spherical metal particles with controlled size, size distribution, and number density, resulting in films with differentiated morphologies and optical properties is discussed.

In recent years, increasing attention and efforts have been devoted to the controlled synthesis of nanostructured materials. The nanostructure plays a fundamental role in determining electronic, optical, magnetic, and mechanical material properties. It is in principle possible to engineer new functional systems by carefully tailoring their structure at the atomic and nanometer scales. One of the more exciting routes adopted to synthesize nanostructured thin films is the controlled assembling of clusters.

Among different chemical and physical assembling techniques, laser processing plays an important role: laser ablation, pulsed laser deposition, laser micromachining, laser etching, and laser-assisted chemical vapor deposition are only some

P.M. Ossi (✉)
Dipartimento di Energia, Politecnico di Milano, Italy
e-mail: paolo.ossi@polimi.it

examples of recently introduced techniques that are reviewed with emphasis on the degree of control of the resulting artificial nanostructures.

7.1 Introduction

The word nanostructure is largely used in the scientific and technical literature with a variety of meanings. In the initial part of this chapter, by nanostructure, we mean the result of the assembling procedure, with a bottom-up strategy of nanometer-sized particles, or briefly nanoparticles (NPs). Thus, our attention is focused onto the mechanisms whereby NPs are formed in a laser-generated plasma. Our goal is to identify conditions suitable to drive the synthesis of NPs with controlled properties and their assembling in an organized, convenient spatial disposition, up to a cluster-assembled (CA) film. Particle properties of interest range from the size and its distribution, to the composition, the chemical and thermal stability, the transport, mechanical, and chemical properties with their peculiar size dependence.

The plasmas produced by laser ablation yield large amounts of particles with typical size in the few nanometer range [1, 2]: the possibility to separately manage laser pulse features, irradiation geometry and radiation – matter interaction allows modifying the complex dynamics within matter ejected from the irradiated target surface. Thus, it is possible to understand and in part to control the mechanisms of NP formation and their relative efficiency.

We move from the considerable activity of the last decade on NP synthesis following irradiation of a solid target with laser pulses, to underline some differences between femtosecond (fs) and nanosecond (ns) pulses that have important effects on NP synthesis. A femtosecond pulse releases its energy to matter adiabatically with respect to thermal conduction. Thus, an intense, ultra-short pulse locally brings to supercritical conditions the target while it preserves a solid density. The extreme temperature – pressure regions explored, together with the fast-quenching conditions associated to material expulsion, constitute ideal conditions to synthesize metastable phases otherwise unattainable. Further to this, ultrashort pulses do not interact with the material ejected from the target; therefore the fundamental thermodynamics – hydrodynamics of NP formation can be considered. By contrast, pulses lasting picoseconds or longer times strongly interact with the nascent high-density cloud of matter evaporated from the target. The resulting photoionization and collisional heating mechanisms have significant effects on particle formation.

In fs ablation, NP formation usually occurs during free plasma expansion *in vacuum*: hydrodynamics suggests that the severe strain experienced at very high strain rate by a rapidly expanding, highly pressurized fluid leads to mechanical fragmentation: such a mechanism is essential to *quantitatively* interpret NP formation [3]. By contrast, an *ambient gas* strongly favors NP synthesis in ns ablation [1]: clustering of species in the expanding plume critically depends on the relative weight of interaction mechanisms between ablated species and ambient gas, including scattering, slowing down, diffusion, recombination, shock wave formation, and

propagation. All these mechanisms are affected by ambient gas nature and pressure. The above differences suggest to separately discuss NP formation when ns and fs laser pulses are used.

For both irradiation timescales to manage the production of NPs, it is essential to know *how* and *when* they are formed. This is our goal. A difficulty to answer such questions stems from a long-standing separation between two approaches to analyze pulsed laser ablation experiments. On the one hand, film properties are correlated to deposition parameters such as target to substrate distance, laser wavelength, fluence, intensity at the target surface, number of pulses [4, 5], atomic mass, and pressure of the ambient gas [6]. On the other hand, plasma expansion dynamics is studied. Several time- and space-resolved plasma diagnostics yield details on the dynamics of the vaporized species escaping from the target: they include optical emission spectroscopy (OES) [7], optical time of flight measurements (TOF) [8], Langmuir probes [9], and fast photography, using an intensified charge coupled device (ICCD) [1, 10], from which plasma front position and velocity are obtained, besides the size and shape of the expanding plasma. Although the two classes of investigations are complementary to each other, only recently plasma plume studies were carried out at conditions suitable to have a feedback on film deposition.

We first review the phenomena associated to the propagation through an ambient gas of a plasma plume produced by a nanosecond laser pulse. The strengths and weaknesses of the most popular models adopted to interpret plasma expansion are recalled and the phenomenological model of mixed-propagation for plume dynamics in the ambient gas is introduced. Recent results on the deposition under different conditions of CA films of carbon, tantalum, and silver are interpreted. It is shown that the average NP asymptotic sizes deduced by mixed-propagation model, agree with those of *as-deposited* NPs, measured by transmission electron microscopy (TEM). The morphology, as investigated by scanning electron microscopy (SEM) and the related optical properties of deposited silver films evolve through well-differentiated stages that were controlled by changing the number of laser pulses and the ambient gas pressure. Selected experimental results on NP formation upon fs ablation mainly of elemental targets are presented, highlighting the nature and the dynamic properties of plasma constituents. The data are discussed in the frame of current models and simulations to describe the mechanisms of ultra-fast ablation relevant to NP synthesis.

7.2 Fundamentals

7.2.1 Plasma–Gas Interaction at Increasing Gas Pressure in ns PLD: Experiments and Modeling

When a laser pulse is absorbed by a solid target, the irradiated surface undergoes intense heating at a rate of the order of $10^{12}\,\mathrm{Ks}^{-1}$ in most materials and violent matter evaporation occurs: a high density, strongly anisotropic vapor cloud

is formed, which lies just above the irradiated surface. Initially, the vaporized matter behaves like a high pressure, high temperature, strongly collisional fluid interacting with the laser radiation. An isothermally expanding plasma results up to the pulse end. Heavy laser – plasma interaction, triggered by intense ionization of plasma species, stimulates additional plume expansion. Particle ejection from the target surface stops at the end of the laser pulse.

Both in vacuum and at low ambient gas pressure (up to about 1 Pa), plasma propagation is similar to a supersonic free expansion with a *linear* relation between the delay time and the position of plume front [11]. Ablation can be considered as an extension of thermal desorption, monolayers being evaporated from the target surface one by one under quasi-equilibrium conditions. A condensation model [12] explains the presence of nanoparticles in the plume, of which they are a minor constituent.

When gas pressure increases, the collisions between the species ejected from the target and ambient gas atoms slow down plume propagation and lead to *shock wave* formation. The high density of the surrounding gas makes plume braking most relevant in the direction normal to the target as compared to the radial directions. Thus, the observed shape of the propagating plume rapidly tends to *spherical*. At relatively low (below 10 Pa) ambient gas pressure, the *initial* plume expansion is similar to that in vacuum [13], but at times longer than 1 μs at most, ambient gas spatially confines the plume, and a slowing down of its front is observed [14]. At larger times plume sharpens and its front shows an oscillatory behavior persisting up to ambient gas pressures of a few tens of Pascal. Generally, the effect occurs at earlier times with increasing gas pressure. At ambient gas pressures beyond about 10^2 Pa, plasma oscillations disappear.

In Fig. 7.1, pictures taken at the same delay times of C plumes ablated from a graphite target allow for comparing propagation in vacuum (Fig. 7.1a) to shock wave formation during expansion in N_2 at a pressure of 13.3 Pa (Fig. 7.1b). The role of ambient gas mass is clear from Fig. 7.1c, where the plume expands in a N_2+Ar (1/9) mixture, at the same total pressure as for the propagations in Fig. 7.1b.

At intermediate gas pressures, between 30 and 50 Pa, plume sharpening is associated to increasing confinement of the emission to plume front. In this pressure range, the slowing down of plume front begins after a few microseconds and continues until a stationary behavior is achieved. At the same time, the rear edge of the plume moves *backwards* towards the target. Such a behavior marks a transition to a *diffusion-like* propagation of plume species through the ambient gas typical of longer times, for pressures in the tens of Pascal range. During this stage, the plume is characterized by important interpenetration of plasma species and ambient gas that leads to plume *splitting*, besides sharpening [15]. Ions and neutrals split into *two* velocity populations. The faster group, which travels practically at the same velocity as in vacuum, consists of particles that move through the ambient gas nearly collision less. The dynamic properties of the slower, delayed population result from the interaction between ablated species and background gas atoms. The effect was observed by TOF distribution analysis of the ablated species and affects both ions [16] and neutrals [17]. During the regime of mutual penetration of the laser-generated plasma and ambient gas, a considerable fraction of kinetic energy is

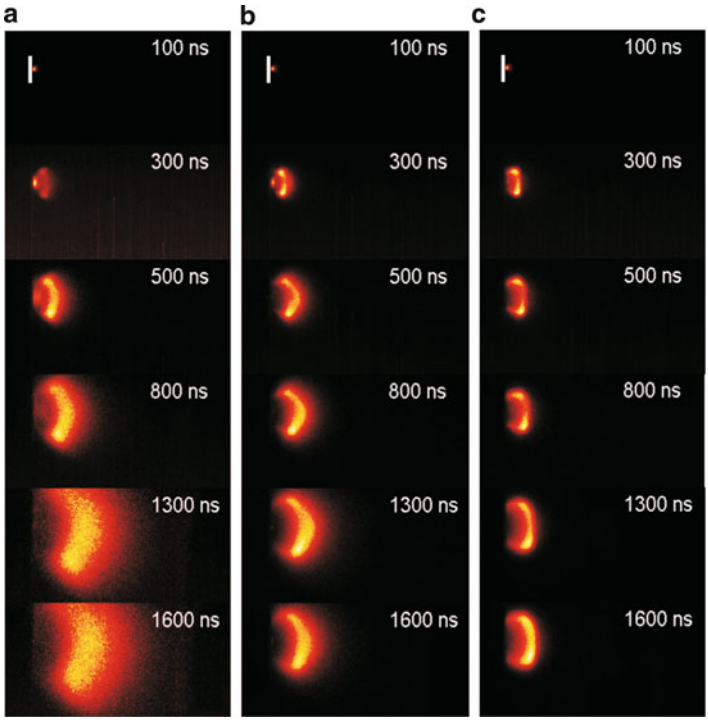

Fig. 7.1 ICCD fast photography pictures of C ablation plumes expanding from a high purity graphite target irradiated with pulses from a KrF excimer laser (wavelength 248 nm, pulse width 25 ns, repetition rate 10 Hz, fluence 2.0 J cm^{-2}). The bars mark the position of target surface. The laser beam was focused at an incident angle of 45° onto the target, placed on a rotating holder. Ablation was carried out: (**a**) in vacuum (residual pressure better than 1×10^{-4} Pa); (**b**) in high purity N_2 ambient gas at 13.3 Pa; (**c**) in mixed N_2+Ar atmosphere, with pressure ratio 1/9, at 13.3 Pa total pressure. Notice the different evolution of plasma size and shape, indicating different degrees of plasma confinement and the development of a shock wave (courtesy of Dr. S. Trusso, CNR-Istituto per i Processi Chimico-Fisici, Sez. di Messina, Italy)

converted into heat, in turn increasing both gas and radiation temperature. At pressures around 10^2 Pa, *turbulence* is observed in the decelerating plume front [18]. By further increase of the gas pressure, the mutual penetration zone contracts and the plasma front is compressed.

The above-illustrated path of propagation behavior of the ablation plume is met independently of the specific combination target – ambient gas – process conditions, although the pressure ranges typical of the different propagation regimes are quite broad and not always the complete sequence of phenomena just discussed is observed.

The interaction of the ablation plasma with an ambient gas is by far a more complex gas dynamic phenomenon than an expansion into vacuum. The gas affects plume dynamics and the spatial distribution, kinetic energy, and kinetic energy distribution of its constituents. As a consequence, cluster nucleation and evolution, as well as cluster energy distribution in the plume are influenced.

When the mass m_g of ambient gas displaced from plume periphery is at least comparable with plume mass M_p, we observe relevant deviations from free expansion of the plume [12]. For a supposed hemispherical plume, the radius r_p is related to plume mass and gas pressure as

$$r_p = [(3M_p k_B T_g)/(2\pi m_g)]^{1/3} p_g^{-1/3}, \tag{7.1}$$

with k_B the Boltzmann constant and T_g, p_g the ambient gas temperature and pressure.

Considering the features of plume expansion, it is unrealistic to search for a single model with general validity to accurately describe the whole above phenomenology, and each analytical model is adequate to represent a specific expansion stage.

Historically, three *analytical* models, the *drag* model [19, 20], the *shock-wave* model [12, 20], and the *diffusion* model [21] were introduced. Summarizing from a recent review [22], drag model, particularly in its delayed version [20], fits well the *early* plasma expansion stage, but when gas pressure and time exceed about 10^2 Pa and about 4 μs, respectively, plume velocity is underestimated. The plume is expected to stop at a distance $x_{st} \cong 4 - 5\lambda$ from the target [23], with $\lambda = (n_g\sigma)^{-1}$ the mean free path of the ablated species in the gas, σ being the relevant scattering cross section. Therefore, beyond a lower threshold value, ambient gas pressure gives rise to a nonlinear dependence of the position of plasma front edge on the distance from the target. Shock wave model, again in the delayed version [20], fits experimental data at *large* values of time and ambient gas pressure. The classical diffusion model [21] systematically underestimates the distance traveled by the plume.

A few gas-dynamic *numerical* models [23–25] fit specific experiments, but their applicability is limited by the specific validity of the required approximations and the complexity of the mathematical treatments.

The analytical models just recalled offer *a posteriori* interpretations of experimental data, yet they have no predictive capability concerning plasma dynamics, due to their dependence on numerical fitting parameters. We now move to a two-stage analytical approach that describes plume propagation under rather wide conditions. We take into account that the high values of temperature and particle number densities in the first stage of plasma propagation [23], with the associated quasi-explosive initial plume expansion, result in a Knudsen layer [26] where the leading contribution is the particle flux velocity. We assume that the particles ejected from the target, with a dominant velocity component directed normal to the surface, undergo diffusive motion. This corresponds to diffusion through the ambient gas whose *effective* number density n_{eff} is considerably reduced with respect to the value n_g deduced from gas pressure p_g. In the resulting *modified diffusion* model, the diffusion coefficient [27] is

$$D' = K\lambda v_0 = K v_0 (n_g\sigma)^{-1}, \tag{7.2}$$

where v_0 is the ejection velocity from the target of the *fastest* group of ablated particles. v_0 is obtained from the initial slope of the measured distance – time curve

for plumes produced and propagating under specified conditions. The choice of the particle group with maximum flux velocity v_0 instead of the usual thermal velocity v of the particles is an *ansatz* of the model to enhance the relevance of flux velocity. Although plume front slows down during expansion (see Figs. 7.2 and 7.3 below), modified diffusion model fits reasonably well experimental data, particularly beyond the initial plume expansion stage. This means that flux velocity indirectly affects plume propagation also at comparatively *large* distances from the target.

For elemental C, Si, Sn, Ag, Ta, and W targets, literature data on the velocity of expansion through different gases of UV laser-generated ablation plumes were analyzed. The integer K values that better fit the data scale with the target atomic mass, from $K = 2$ (light elements: C, Si) to $K = 6$ (intermediate mass elements: Ag, Sn) to $K = 8$ (heavy elements: Ta, W). Thus, given the target mass, K value is *uniquely* identified.

To reproduce the experimentally observed initial linear behavior of plume expansion (see, e.g., [28] for C), drag model is most suited. We study for simplicity a one-dimensional plume expansion along the principal plume axis x. When we consider the diffusion dynamics of a fluid of classical particles in the presence of viscosity, whose effect is embodied in a coefficient ξ [29] (ξ is a diffusion coefficient multiplied by time), with the initial conditions $x(0) = 0$ and $(\mathrm{d}x/\mathrm{d}t)(0) = v_0$, the position $x(t)$ of an atom is

$$x(t) = \frac{v_0 D'}{\xi}\left[1 - \mathrm{e}^{\left(-\frac{\xi \cdot t}{D'}\right)}\right] \tag{7.3}$$

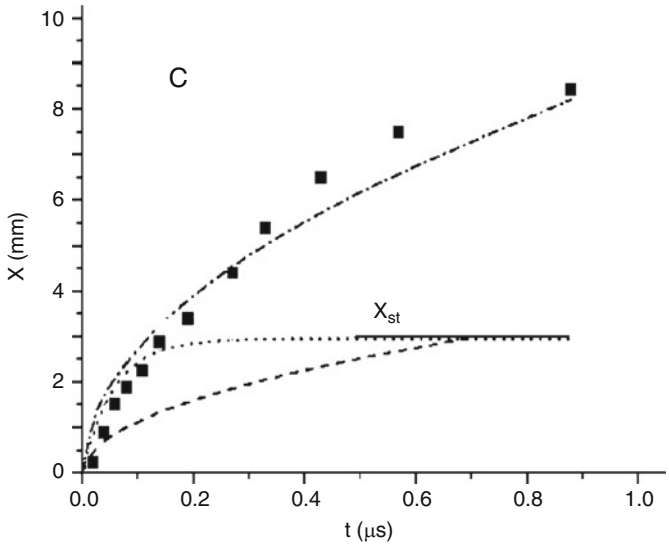

Fig. 7.2 Position x (*full squares*) of the front edge of carbon plumes propagating through N_2 [28] as a function of time. *Dashed curve*: diffusion model; *dashed-dotted curve*: modified diffusion model; *dotted curve*: modified drag model. x_{st}: stopping distance

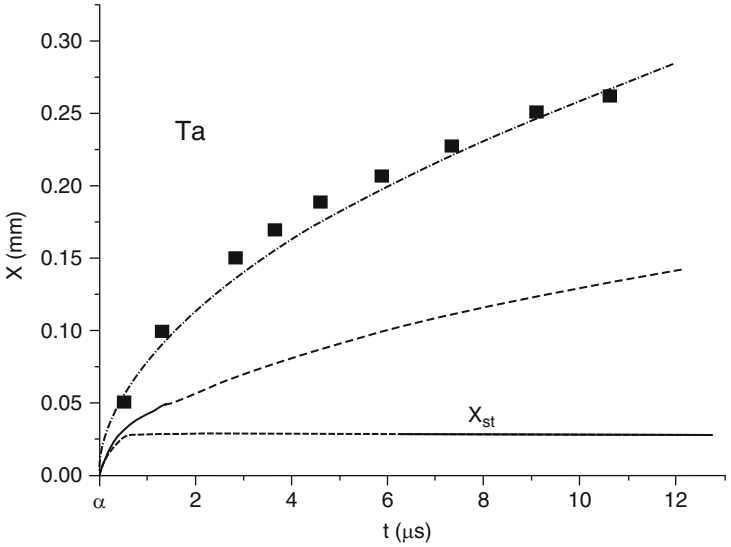

Fig. 7.3 Model analysis of tantalum plume propagation through O_2 vs. time [35]. General information as for Fig. 7.2

Equation 7.3 describes *modified drag* model, where both the slowing down coefficient $b = \xi D'^{-1}$ and the stopping distance $x_{st} = v_0 D' \xi^{-1}$ have a clear physical meaning.

Initially, the number density n_a of the ablated particles is larger than n_g, but the fast plume expansion leads to the condition $n_a = n_g$, corresponding to the formation of a stable shock wave front and to a change of expansion regime. The inequality $n_a < n_g$ is established in the body of the plume and ambient gas atoms are heavily scattered by fast plume constituents (normally, positive ions) that are slowed down and *aggregate* themselves with the slower particles initially grouped in the plume body and tail.

The sequence of such complex phenomena is mimicked combining modified diffusion and modified drag models that result in *mixed-propagation model*. The unphysical discontinuity of plume propagation at x_{st} coincides with the region where the viscous slowing down of plume front leads to formation of a stable shock wave front. At distances $x < x_{st}$ modified drag model holds, while for $x \geq x_{st}$ modified diffusion model holds. The x_{st} value is chosen according to the estimate $x_{st} \cong 4\lambda$ [23] and it is calculated using the n_g and pertinent σ values.

At ambient gas pressure lower than 1 Pa, x_{st} is often much larger than the usual values of target to substrate distance x_{T-S} (a few centimeters) and modified drag model is adequate to describe plume dynamics.

Mixed-propagation model has been tested against literature data on the dynamics of ablation plumes from different targets, propagating in different ambient gases at various pressures [30–34]. The model offers a highly simplified description of plasma expansion, but its easily accessible input parameters v_0, σ, n_g, and n_a make it

Table 7.1 Collection of data from ablation experiments on C [28], Ta [35] and Ag [34]

Target	λ (nm)	E(J cm^{-2})	τ (ns)	x_{t-s} (mm)	p_g (Pa)	T(K)	n_g (cm^{-3})
C	248	38	20	50	30; N_2	300	7.2×10^{15}
Ta	532	5.0	6	30	20; O_2	300	4.8×10^{15}
Ag	248	2.0	25	35	10; Ar	300	2.4×10^{15}
					40; Ar		9.7×10^{15}
					100; Ar		2.4×10^{16}

Table 7.2 Collection of parameter values for mixed-propagation model (see text)

Target	$< n_a >$(cm^{-3})	σ_{a-g}(cm^2)	σ_{a-a}(cm^2)	$< v >$ (cm μs^{-1})	t_f (μs)	x_{aggr} (cm)
C	1.7×10^{17}	7.4×10^{-16}	1.5×10^{-15}	4.5	1.8	2.5
Ta	5×10^{15}	3.7×10^{-15}	7.5×10^{-15}	0.7	0.7	3.3
Ag_{10Pa}	7.1×10^{14}	3.8×10^{-15}	3.7×10^{-15}	0.5	0.8	0.7
Ag_{40Pa}	1.4×10^{15}	3.8×10^{-15}	3.7×10^{-15}	0.3	3.3	0.5
Ag_{100Pa}	2.8×10^{15}	3.8×10^{-15}	3.7×10^{-15}	0.2	7.4	0.4

useful to predict general trends of plume behavior. Here, we discuss the propagation of C in molecular nitrogen [28], Ta in molecular oxygen [35], and Ag in argon [34]. In Tables 7.1 and 7.2 are collected data from ablation experiments and parameter values used in mixed-propagation model, respectively.

In Fig. 7.2, data on the propagation of the front of carbon plumes in N_2 (full squares) [28] are compared with predictions of diffusion model (dashed curve), modified diffusion model (dashed-dotted curve), and modified drag model (dotted curve). The latter fits well the first stage of plume expansion. It predicts that plume is stopped at x_{st}. Diffusion model appears inaccurate. Its modified version well fits the data at intermediate and delayed times, but slightly overestimates plume expansion velocity in the neighborhood of the target. From a fit on available data [36, 37] on carbon ablation with excimer lasers in vacuum, or at low ambient gas pressure, over the energy density interval between 1 and 10^2 J cm^{-2}, the initial velocity is $v_0 = 5.2\,\text{cm}\,\mu\text{s}^{-1}$. Mixed-propagation model successfully fits experimental data on carbon plume expansion for different gas pressures and laser energy densities (50 Pa, 12 J cm^{-2} [28]; 66 Pa, 6 J cm^{-2} [38]). Taking $x_{st} = 4\lambda$, an estimate for the slowing down coefficient is obtained from $b = v_0(4\lambda)^{-1}$. For C, $K = 2$.

In Fig. 7.3 are displayed the results of the fitting procedure to the expansion of tantalum plumes in oxygen [32, 35], starting from optical emission spectroscopy data. The v_0 value used in the fits is $1.5\,\text{cm}\,\mu\text{s}^{-1}$ [35] and $K = 8$. The trend of the fits is similar to that discussed for carbon. No data are available on the early plume expansion stage of Ta. Experimental data fall beyond the stopping distance x_{st} so that modified diffusion model is enough to describe plume dynamics. The fit obtained by mixed-propagation model is of equivalent quality to that of the literature analysis [35].

For silver fast photography pictures of the laser-generated plasma at several time delays were analyzed: from a fitting on propagation distances traveled by plume front versus time in the initial, linear plasma propagation stage v_0 values of 1.11,

1.04, and 0.86 cm μs^{-1} were obtained for expansions in Ar at 10, 40, and 100 Pa [34]. The adopted K value is 6.

For the discussed targets, mixed-propagation model fits to experimental data are of accuracy comparable, or slightly better than existing approaches. The model can be applied to analyze data obtained for a wide range of ablation conditions and it does not require fitting parameters, apart from K, whose value can be easily chosen, as discussed. The results of mixed-propagation model are particularly useful as input parameters to model the growth of nanoparticles in the expanding ablation plasma.

7.2.2 Nanoparticle Synthesis

We focus on low-energy landing (energy of the order of fractions of eV at.$^{-1}$) of plasma plume onto the substrate. In such conditions, the particles possibly carried by the plume diffuse and aggregate together on the substrate surface [39] until, beyond a critical degree of surface coverage, coalescence in larger NPs occurs. Such a deposition path is attractive to produce CA materials that can "remember" the properties of their precursor building blocks. In spite of being an important parameter, the kinetic energy of the deposited species was rarely allowed for. In particular, the kinetic energy of Au species was changed from several tens to fractions of eV at.$^{-1}$ by adjusting gas pressure and target to substrate distance in PLD experiments [40], but neither evidence of fragmentation nor of soft landing of the particles following impact onto the substrate was reported.

CA Pt films deposited changing both the kinetic energy of the plume and the number of laser pulses, thus changing the degree of substrate coverage with NPs, were later observed by STM [41]. The average particle diameter increases with increasing film thickness, following a power law with an exponent similar to that observed for metals grown by MBE. This is taken as evidence that NPs grow *on the substrate* by surface diffusion of the deposited material.

Nucleation and growth up to a critical particle size, followed by coalescence and coarsening at large degrees of substrate coverage drive the growth of Cu nanocrystals with size below 10 nm synthesized in nanocomposite films deposited by PLD in argon at low pressure, not exceeding 0.66 Pa. At higher ambient gas pressures, up to 13 Pa, again nucleation and growth mainly occur at the substrate, but the reduced surface mobility inhibits the coarsening stage, so that highly anisotropic nanocrystals form [42]. The same scheme of NP growth was reported for Fe/Mo [43], Fe/Cu(111) [44], and Au in amorphous Al_2O_3 layers [45].

By contrast, in a careful analysis of the growth of silicon NPs with narrow size distribution [46], plasma spectroscopy shows that NP nucleation and growth occurs *in the expanding ablation plume*. A more recent deposition and modeling study [25] confirms that Si NPs are nucleated and grow in the plume. Ionization processes occurring when plume propagates through an ambient gas result in very high nucleation rates and small cluster critical radii. The synthesis of C NPs in plumes expanding through He and Ar atmospheres up to pressures as high as 1 kPa was

reported and modeled [30], again keeping into account the relevant role of ionization phenomena in the interface region between the shock wave front and the ambient gas [47]. Cluster-assembled W films were deposited in different atmospheres and pressure ranges [48]. The surface morphology, bond coordination, and oxidation path of the deposited films, both when exposed to ambient atmosphere and when synthesized in dry air, were systematically studied and complement a detailed HREM analysis of structure, size, and morphology of the deposited clusters [49]. Ag nanoparticles were synthesized in a controlled way in He [50] and Ar [34] over wide pressure ranges. Scanning and transmission electron microscopy images of the samples show that they belong to CA materials. Both the growth path followed by the films, as revealed by the surface morphology and the measured NP sizes, convey a coherent picture whereby NPs form in the expanding ablation plume.

In the framework of this picture, using the parameters calculated in the analysis of plasma propagation by mixed-propagation model, the average NP asymptotic size, which is the number N of constituent atoms in a particle that reached a steady state during plume propagation, is evaluated.

It is commonly observed that NP formation proceeds through the steps of nucleation, growth, and cooling [51]. The presence of an ambient gas requires solving a set of hydrodynamic equations for plume expansion, including vapor condensation. Such an approach is out of the present calculation capability. We assume an initial seed population of tiny clusters [52] in the propagating plume. Their existence is most likely, given the high ionization degree of the plume and the ion tendency to be surrounded by neutral atoms [25]. For given ablation conditions (see Table 7.1 for the examples discussed here), the average *asymptotic* number N of atoms in a NP that attained a steady state during plume expansion is calculated in the ideal gas approximation. The plume experiences a range of internal pressures and is spatially inhomogeneous, so that growing NPs at different stages of evolution coexist in it; yet we consider averages over long times. N is given by

$$N = (\langle n_a \rangle \cdot \sigma_{a-a} \cdot \langle v \rangle \cdot t_f) \cdot (n_g \cdot \sigma_{a-g} \cdot \langle v \rangle \cdot t_f) \cdot x_{T-S} \cdot x_{aggr}^{-1} \tag{7.4}$$

when the target to substrate distance x_{T-S} is shorter than the distance x_{aggr} over which NPs grow in the expanding plasma and

$$N = (\langle n_a \rangle \sigma_{a-a} \langle v \rangle t_f)(n_g \sigma_{a-g} \langle v \rangle t_f), \tag{7.5}$$

when x_{T-S} is larger than x_{aggr}.

In both equations, the distance x_{aggr} traveled by the plume during particle growth is deduced from optical emission data, considering the relevant species in the plume (such as TaO, for Ta ablation [35]). When such data are lacking, we adopt the relation [22]

$$x_{aggr} = 6 p_g^{-1/5}. \tag{7.6}$$

Equation (7.6) gives an upper limit for the value of x_{aggr}. The monotonic dependence of particle size on p_g in (7.6) agrees with a number of results on Si [4, 25], in turn

well fitted by mixed-propagation model [32]. Yet we notice that the size of Si NPs grown in helium at pressures as high as 1 kPa shows a peaked dependence on gas pressure, with a maximum at about 600 Pa [53]. The choice of the value of x_{aggr} is a delicate point of mixed-propagation model, as we noticed when the measured sizes of dispersed silver nanoparticles deposited on suitable TEM grids were compared to the calculated values obtained by the model [34]. An excellent agreement was found choosing x_{aggr} as the distance at which the absolute plasma luminosity decays by three orders of magnitude with respect to the initial value. It is likely that at such a distance from the target, the plasma is non-collisional, so that at x_{aggr}, the NPs in the plume reached a steady size.

In (7.4) and (7.5) the particle formation time t_f is the time needed by the plume to travel the distance x_{aggr}. The average number density of ablated atoms $< n_a >$ is obtained from the ratio between the number of ablated atoms per pulse and the volume of the plume, deduced from fast imaging pictures of the plume taken both near the target and at a distance from the target around x_{aggr}. Increasing $< n_a >$, the collision rate between ablated atoms increases, while increasing n_g, the plume becomes more confined. Both trends favor NP formation and growth. σ_{a-a} and σ_{a-g} are the geometric cross sections for ablated particle – ablated particle and ablated particle – gas atom binary collisions. A unity sticking coefficient is assumed. Although both for ambient gas atoms and for ablated species velocity distributions should be considered, the velocity v_0 for ablated particles and the average velocity v_g for gas atoms, as deduced from the gas temperature, are assumed. The average between v_g and v_0 is taken as the representative average velocity $< v >$ of plume particles, being the impact velocity in a binary collision between a slow gas atom and a fast plume particle. With this choice, an important role in particle formation is attributed to the fastest group of ablated particles. When $< v >$ increases, the time interval between two subsequent collisions decreases, thus increasing the rate of NP growth.

In both (7.4) and (7.5), the first term ($< n_a > \cdot \sigma_{a-a} \cdot < v > \cdot t_f$) yields cluster growth and is proportional to the scattering probability between ablated particles, while all the mechanisms resulting in slowing down and confinement of the plume are embodied in the second term ($< n_g > \cdot \sigma_{a-g} \cdot < v > \cdot t_f$), which is proportional to the scattering probability between ablated particles and gas atoms.

In the first stage of plume propagation, atoms mainly aggregate together and NPs grow. Beyond the distance x_{aggr}, particle cooling, both by a dominant evaporative and by a less effective collisional mechanism, *balances* particle growth. The term $x_{T-S} x_{aggr}^{-1}$ in (7.4) and *1* in (7.5) takes into account the competition between growth and cooling mechanisms in a particle, by avoiding an indefinitely persisting, unphysical particle growth when the plume propagates over large distances, as described by (7.4).

The phenomenological model we just described for NP growth in the expanding ablation plasma is highly simplified. The contrasting experimental results on Si, the only material whose behavior was studied with some detail, although not exhaustively, indicate that the dependence of x_{aggr} on laser fluence and on ambient gas nature and pressure is a complex one. This suggests that our understanding

Table 7.3 Asymptotic number of atoms per NP, N and average NP diameters, d calculated with mixed-propagation model. For comparison, available NP diameters measured by TEM are reported

Target	p_g (Pa)	N	d_{th} (nm)	d_{exp} (nm)
C	30; N_2	5.5×10^4	10	5 ÷ 10 [30]
Ta	20; O_2	9.6×10^4	17	–
Ag	10; Ar	15	0.7	0.9 ÷ 1.7 [34]
Ag	40; Ar	158	1.7	1.8 ÷ 2.2 [34]
Ag	100; Ar	2.34×10^3	4.1	4 ÷ 7 [34]

of the combined effect on particle formation of the parameters that drive plume propagation is far from being complete.

The model of NP growth was applied to evaluate the average asymptotic *size* of NPs grown in ablation plumes of C, Ta, and Ag, propagating under the experimental conditions listed in Table 7.1. Parameter values for mixed-propagation model from Table 7.2 were used in the calculations. In all cases, x_{T-S} is larger than x_{aggr}, so (7.5) holds. The average number of atoms per particle N is reported in Table 7.3 together with the average diameter of spherical NPs: in the calculations, we used packing efficiency $\eta = 0.67$ for close-packed noncrystalline structures, based on NP structure from electron diffraction patterns taken on samples observed by TEM.

From Table 7.3, there is a reasonable agreement between calculated and observed NP sizes, when available. The effectiveness of gas pressure to NP growth is evident in the case of Ag films pulsed laser deposited keeping identical all other process conditions.

Thus, although blind with respect to the detailed interaction mechanisms among particles in the ablation plasma that propagates through the ambient gas, mixed-propagation model appears to have a degree both of interpretative and of predictive ability concerning NP growth in the expanding plasma produced by a nanosecond laser pulse.

7.2.3 *Controlled Deposition of 2D Nanoparticle Arrays: Self-Organization, Surface Topography, and Optical Properties*

We now discuss the synthesis and deposition of silver NPs produced by laser ablation in a controlled inert gas (Ar) atmosphere to show up to what extent is it possible to manage the deposition of a spatially organized two-dimensional arrangement of NPs with controlled properties (size, size distribution, number density). Selected physical properties of the obtained film can thus be tailored. As an example, the position and the full width at half maximum (FWHM) of the surface plasmon resonance of the Ag films is considered. Our study combines an investigation of plasma expansion dynamics by fast photography imaging with the modeling of NP growth by mixed-propagation model and with electron microscopy observations, both SEM

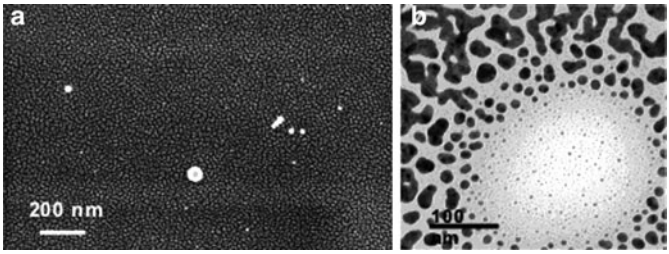

Fig. 7.4 Representative pictures of a silver film deposited at $p_{Ar} = 10$ Pa showing: (**a**) the surface morphology (SEM); (**b**) the nanostructure (TEM) [34]

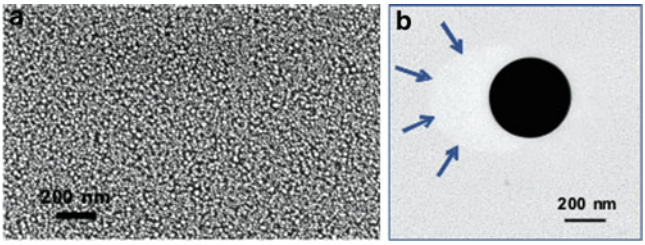

Fig. 7.5 Representative pictures of a silver film deposited at $p_{Ar} = 100$ Pa showing: (**a**) the surface morphology (SEM); (**b**) the nanostructure (TEM) (adapted from [54])

and TEM of the morphology and nanostructure of the deposited films, whose optical properties were tested by UV-vis spectrophotometry [34, 54].

For all depositions, the number of laser pulses was fixed at 10,000 and the process was stopped before the substrate surface were completely covered. In Fig. 7.4 are shown representative SEM (Fig. 7.4a) and TEM (Fig. 7.4b) pictures from the sample deposited at the lowest pressure $p_{Ar} = 10$ Pa. Film morphology consists of silver islands with smooth rounded edges, with typical size in the range of few tens of nanometers. The elongated shape of most of such islands indicates that they result from *coalescence* of definitely smaller, nearly spherical particles, some of which can be still observed as isolated NPs on the film surface. A similar morphology is observed in the sample grown at $p_{Ar} = 40$ Pa. The TEM picture in Fig. 7.4b clearly shows structures resulting from a coalescence process. Besides them, in the circular, near-center region of the image, spherical, isolated NPs with the smallest size visible to the naked eye are visible. The spatial density of the latter is low, probably due to the shadowing effect of a big spherical droplet that masked a portion of the substrate during part of the deposition process. We conclude that in the films deposited at the lower ambient gas pressures, the adopted number of laser pulses results in a particle density on the substrate surface large enough that aggregation of small NPs occurs, giving rise to coalescence into the observed big NPs besides the smaller spherical ones.

Turning to the surface of the sample grown at $p_{Ar} = 100$ Pa (Fig. 7.5a), it is mostly covered by a random distribution of *isolated* sphere-like NPs. There is

no evidence for a coalescence process. In a film grown at $p_{Ar} = 70\,Pa$, a similar morphology is observed [54]. In the corresponding TEM picture in Fig. 7.5b, only near-spherical, small NPs are visible, most of them having size, evaluated by a counting software [55] in the range between 3 and 5 nm; some particles composed by two or more smaller spherical NPs can be observed. In Fig. 7.5b, three regions can be discerned. The black circular area is a micrometric droplet ejected by the liquefied target surface by pressure recoil that gently landed on the substrate surface during NP deposition. The arrows indicate the boundary between a crescent-shaped area, adjacent to the droplet on the left side, and the remaining sample area. Both these zones are covered with isolated, small, spherical NPs with quite narrow size distribution. Within the crescent, the NP number density is evidently lower than in the remaining area. The gradient of NP number density on moving away from the droplet indicates that it severely shadows a fraction of the particle flux directed at the substrate, the mechanism becoming less and less relevant on moving away from the center of the normally projected droplet shadow. Thus in a single picture, we look at snapshots of film growth at *different times*. The same reasoning holds for Fig. 7.4b. In the early stage of deposition on the substrate isolated, nanometer-sized particles are present. With increasing deposition time, NP size increases until they begin to coalesce, giving rise to larger islands that lose spherical symmetry, until lastly a percolated structure results.

It is noticeable that in the films deposited at high Ar pressures, the shape of nearly all NPs is sphere-like. For the films deposited at lower gas pressures, where particle coalescence dominates, only a *minor* fraction of *spherical* particles was identified. NP sizes reported in Table 7.3 refer to such particles.

In all the above films, most likely NPs of size near those calculated by mixed-propagation model constitute the building blocks from which kinetics and, to a lower extent, thermodynamics drive the formation of a CA film, as shown by the discussed morphology.

While mixed-propagation model that is based on the kinetic gas theory nicely predicts NP size, it does not include the kinetic evolution of mutually interacting particles on the substrate. However, some observations are in order. In particular, the adsorption energy of Ag on most substrates is low, so that also the initial sticking probability is low [56]. Thus most likely, Ag *films* grow according to the Volmer–Weber scheme, forming three-dimensional islands. The observed coalescence in the films deposited at low Ar pressure can be explained because, at fixed number of laser pulses, the number of Ag NPs impinging on the substrate increases with lowering Ar pressure. Both the progressive increase in NP areal density and the corresponding decrease in NP number density support this picture.

The well-differentiated morphologies of the deposited Ag films, thereby clustered NPs are found at $p_{Ar} = 40\,Pa$, while slightly increasing the pressure up to $p_{Ar} = 70\,Pa$ a population of isolated NPs results open the way to obtain nanostructured metal films with finely tuned optical properties. In noble metals, a surface plasmon resonance (SPR), resulting from the coherent oscillation of surface electrons excited by an electromagnetic field, can be observed. In isolated Ag NPs with size of few nanometers a SPR peak is observed at about 400 nm [57]. The position

Table 7.4 Position ω_p and FWHM of the plasmon resonance peak for Ag films deposited with different process parameters. The films consist of NP arrays whose observed morphologies are reported

p_{Ar} (Pa)	Laser pulse #	ω_p (nm)	FWHM (nm)	Film morphology
10	10,000	632	>630	Percolated
40		560	336	Clustered NPs
100		440	150	NPs

and shape of the SPR peak critically depend on NP size, shape, and spatial distribution [58, 59]. Thus, a fine control of the morphology of a nanostructured thin film allows controlling its optical properties. In Table 7.4 are reported both the position (ω_p) and the FWHM of the SPR peak of samples deposited at different Ar pressures. Keeping fixed the number of laser pulses and decreasing p_{Ar} from 100 down to 10 Pa, the plasmon position red shifts from 440 to 643 nm while its width progressively increases from 150 nm up to more than 650 nm. Such trends indicate that the films deposited at low ambient gas pressure no more consist of isolated, spherical NPs, as confirmed by SEM and TEM pictures.

Thus, in the case of silver deposition, with the adopted parameters, playing with ambient gas (Ar) pressure, a qualitative change in the strategy of self-assembling of NPs on the substrate occurs and involves coalescence. The trend of the measured SPR of the films shows that it is possible to finely tailor the nanostructure of this family of films and concurrently their optical properties.

In conclusion, our comprehension and control of the key mechanisms of NP synthesis by ns laser ablation in an ambient gas is moving towards the stage of identifying experimental conditions suitable to deposit on a substrate arrays of dispersed NPs with predefined size and composition. This is a requisite to finely control the physicochemical properties of such NPs in the frame of a bottom-up strategy.

7.3 NP Formation in Femtosecond PLD: Experimental Results and Mechanisms

The morphology, composition, and nanostructure of films synthesized by femtosecond (fs) PLD of a solid target significantly differ from those of films obtained with ns laser pulses. In most cases, we find random stackings of nanoparticles whose sizes lie between 10 and 100 nm [2] and quite narrow size distributions [10]. By fs ablation, NPs of several elemental materials were obtained in an efficient and chemically clean way. Besides simple (Al [5, 60]), transition (Ti [2, 7], Ni [61]) noble metals (Cu [10, 60], Au [10]) and semiconductors (Si [62]), also compounds even with complex stoichiometry were synthesized as NPs. We mention MgO, $BaTiO_3$, GaAs [62], TiO_x [7], Ru_2B_3, and RuB_2 [63]. The composition of the deposited NPs in relation to that of the target is a still poorly investigated, nontrivial problem, in particular when traces of reactive gases such as oxygen are present in the deposition chamber [64].

Parallel to film deposition attention was focused to plasma analysis, mainly considering the emitted signals that characterize the species escaping from the target, ions, neutrals, and NPs. Pairs of ultrashort, time-delayed pulses were recently used to change the relative proportions and kinetic energies of ions and neutrals with respect to the preformed plasma, thus influencing NP production. The accumulated wealth of data are useful to model the dynamics of plume formation and the early stages of expansion, to identify mechanisms of particle synthesis whose relative weight as a function of irradiation conditions is discussed, often taking the deposited laser fluence E as the reference experimental parameter.

Two conceptual schemes are presently adopted to explain NP synthesis: direct cluster ejection from the target as a consequence of material disruption by a laser-induced explosion-like process, or aggregation in the flying ablation plume via a collisional mechanism [65]. Available models and simulations take care of the features of fs pulse interaction with solid matter, namely an initial ultrafast heating without changing matter density, followed by a very rapid expansion and cooling. Just this sequence is at the roots of NP formation. According to the results of hydrodynamic simulations [66, 67], a thermal wave is followed by a pressure increase and a propagating shock wave. Molecular dynamics (MD) simulations [65, 68] put into evidence mechanisms such as phase explosion, fragmentation, evaporation, and mechanical spallation. Important *quantitative* discrepancies are found when model predictions are compared with experiments, even considering the very ablation depth. This is an indication that ablation mechanisms and their relative weight for various fluence ranges are still partly unknown. In the following, we focus on a selection of reliable results and concepts concerning NP synthesis by ultrafast laser pulses.

Detailed analyses of the ablation plasma produced by ultrashort pulses were conducted mostly on elemental targets irradiated with light visible to near-IR at fluence values ranging from intermediate to modest and laser intensities between a few 10^{12} and a few $10^{14}\,\mathrm{Wcm^{-2}}$. By the time of flight mass spectrometry (TOF-MS), both plasma constituents and their velocity distributions were determined for Si [69]. When fluence is large enough, being above the ablation threshold, the velocity distribution is a full-range Maxwellian whose center-of-mass velocity is attributed to collisions in the Knudsen layer. In metals, Ti being the prototype, again by TOF-MS two components are found in the ion velocity distribution at rather low fluence; kinetic energies of Ti^+ ions in the keV range are taken to indicate that Coulomb explosion could significantly contribute to ablation [70]. Recently, time resolved optical emission spectroscopy (OES) was coupled with fast imaging of the expanding plasma: in Fig. 7.6, images of plasmas produced irradiating the same Si target with ns and fs pulses are compared to each other at comparable delays.

In some cases, the size and size distribution of the deposited dispersed NP populations were measured by atomic force microscopy (AFM). Basically, the same picture emerges: at very short delays, a plume propagates normally to the target with narrow angular aperture. According to OES, the constituents of such a plasma are atomic species, both ions and neutrals. Velocity measurements show that ions are always faster, with velocities of a few $10^4\,\mathrm{ms^{-1}}$, due to their strong coupling to

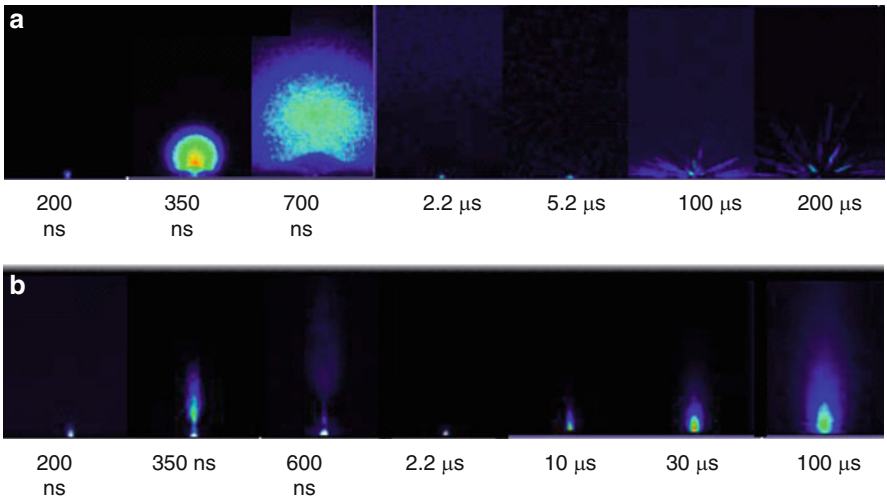

Fig. 7.6 ICCD fast photography pictures of ablation plumes from a silicon target irradiated in vacuum with (**a**), 25 ns pulses, $\lambda = 248$ nm (**b**), 100 fs pulses, $\lambda = 620$ nm (adapted with permission from [64])

electrons that escape first from the target, while atom velocities are about one order of magnitude less. Data are available for Ti [2,71], Zr, Hf [71], Au, Cu [10], Al [60]. In the latter study, plasma expansion was analyzed via space- and time-resolved X-ray absorption spectroscopy, monitoring the energy shifts and modifications of the Al $L_{II,III}$ absorption edge, similarly to an earlier investigation on Si [62].

At delays of the order of microseconds, a second plume with considerable angular aperture and rather low velocity, from a few 10^2 to a few 10^3 ms^{-1}, is observed. A typical *blackbody* spectrum, obtained by OES, leads to consider NPs as the constituents of such a plasma [2, 7, 10, 71]. Whenever film nanostructure was analyzed, SEM or AFM show random distributions of NPs [2, 10, 61]. In these studies, care was taken of depositing a submonolayer to avoid cluster self-organization on the substrate, most likely resulting in coalescence. Since the above observations are independent of the chemistry of the target (metal, semiconductor), the production of NPs appears to be associated to fs ablation.

The reported velocities of the different species are nearly constant up to considerable distances from the target (from 1 mm to centimeters [2]). Qualitatively, the ratio between atom/ion and cluster velocities is correctly reproduced in a direct simulation Monte Carlo (DSMC), where MD results were used as input parameters [72].

For both Au and Cu [10] atom velocities, measured as a function of the fluence, increase near the ablation threshold E_t, presumably due to the increased quantity of ablated matter and the related changes in the adiabatic expansion stage, while NP velocities decrease near E_t, due to changes in their size distribution. The velocities of both populations are nearly independent of fluence at values larger than E_t, showing

that in the *initial* plasma expansion, the average temperature of ablated matter is almost independent of E.

Defining atomization as the direct transformation of target material into the gas phase [73], both in Au and in Cu, the measured ablation efficiency is maximum at the fluence E_{NP} where atomization is minimum. Afterwards increasing E atomization slightly increases [10]. Such a strong correlation is explained in terms of the higher energy cost of atomization, compared to NP production. The E_{NP} value is associated to target heating regime. At fluences larger than the ablation threshold E_t, matter escapes from layers below the target surface that are progressively deeper and colder, so it cannot be energized enough to be fully atomized and a mixture gas – NPs (liquid) escapes from the target. As the ablation efficiency is much higher than the value expected for thermal vaporization (pure atomization), a considerable fraction of NPs is likely to be ejected *directly* from the target.

The shape of the deposited NPs is sphere-like and they belong to two distinct populations [10]; the smaller-sized particles are supposed to be *directly ejected* from the target. The size distribution of the larger particles scales as $r^{-3.5}$, r being their radius. This distribution is observed when a mechanism of fragmenting collisions dominates; thus, such NPs are expected to result from *in-plasma* collisional sticking.

Some attempts were made at manipulating plasma constituents with a delayed fs [2], or ns [61] pulse, playing also with the delayed pulse wavelength [61]. In particular, irradiating Ni with UV fs pulses with $\lambda = 263\,\text{nm}$, the average diameters of deposited dispersed NPs measured by AFM are nearly half of those resulting upon irradiation with identical pulses, with doubled wavelength $\lambda = 527\,\text{nm}$. In both cases, particle size is independent of the laser fluence, up to $1\,\text{J cm}^{-2}$. When a further ns-UV pulse intercepts the ablation plasma at different delays, changes are caused in the size distribution of the deposited NPs. At fixed intermediate fluences (about 0.5 and $0.4\,\text{J cm}^{-2}$, respectively) of the fs and ns pulses, NPs shrink, the effect being more marked at shorter delays. The result suggests that in the expanding plasma, NPs *group together* as a function of their size, the smaller ones traveling ahead of the bigger ones.

It is to be mentioned that at very long delays, of the order of tens of microseconds, when irradiation is performed at high fluences (about $10\,\text{J cm}^{-2}$ and higher), *droplets* can be visible to the naked eye due to their luminous trajectories. Whenever such debris are observed, their fingerprint are micron-sized particles lying on the surface of the deposited films, evident in SEM pictures [62]. The difference in size and velocity between such species and NPs indicates that droplets are not "giant" particles, nor the two species are likely to be produced by the same mechanism. Stress confinement in the target, associated to ultrashort pulses was proposed as their origin [65].

Irrespective of the target nature, a scaling among thresholds in laser fluence holds thereby the thresholds for atomic, E_a and nanoparticle, E_{NP}, emissions are comparable, both being lower than the value E_d for droplet emission [64]

$$E_d > E_a \approx E_{NP}. \tag{7.7}$$

The main experimental results on NP synthesis can be correlated with reasonable agreement to simulations of target behavior under fs pulse irradiation. MD indicates [65] that at high deposited fluences, the main mechanism responsible for material expulsion from the target is phase explosion of matter heated above the thermodynamical critical temperature T_c. The surface region decomposes into a foam of interconnected liquid regions, containing gas molecules, liquid droplets, and small particles. At increasing depth from the target surface where matter decomposition occurs and thus in regions where the degree of overheating is progressively lower, the liquid fraction increases and big droplets form in the tail of the ablation plume. NPs segregate in different regions of the expanding plasma depending on their size, the smallest ones being grouped in the front region, while medium-sized ones are found in the middle. Two particle populations are consistently found, the smaller ones being ejected in the explosive decomposition of matter into liquid and vapor, while the larger ones result from decomposition and coarsening of the transient interconnected liquid regions.

Combining smaller scale MD and larger scale DSMC techniques, two channels of NP production are identified, namely direct ejection following laser–matter interaction and collisional condensation-evaporation in the propagating ablation plume [72]. The processes belonging to the first channel include, besides phase explosion, photomechanical spallation and fragmentation; such *volume* mechanisms produce small particles and atoms/ions.

Gas-phase collisional sticking and evaporations are the processes belonging to the second channel. They resemble those occurring in aggregation sources [74] and are favored by the huge number of seed molecules and small particles in the laser-generated plasma.

Femtosecond Al ablation was investigated in a one-dimensional hydrodynamic numerical model [73] exploring the relative weights of different decomposition processes. Moving from a thermodynamically complete equation of state, the time evolution of heavy particles is followed on a temperature-density (T-ρ) phase diagram, taking into account matter slices lying at different depths below the target surface. Ablation mechanisms are compared to each other as a function of the laser fluence E, allowing for interplay between the kinetic lifetime of the metastable liquid state and the time needed to induce mechanical fracture of the material. Atomization requires the highest initial temperatures, attainable only in a near-surface thin layer, not exceeding 15 nm, so that only a small fraction of matter is ablated via this mechanism. A metastable liquid state forms at depths between 20 and 30 nm where the thermodynamical critical temperature is reached and phase explosion occurs, but also this thermal mechanism involves a limited amount of material. Indeed the molten layer is much thicker, but most particle trajectories, although entering the metastable liquid region, reach temperatures below T_c. Matter persists for comparatively long times in a metastable state and mechanical effects prevail over thermal ones, leading to decomposition into droplets and chunks.

The fractions of material ablated by the above mechanisms depend on target nature and laser fluence E. At low E, target melts; with increasing fluence, material fragmentation [65] occurs, then mechanical and thermal mechanisms coexist, until,

at large E values atomization, phase explosion and mechanical decomposition take place at different depths in the target; the latter mechanism dominates in Al in the interval 0.1–5 J cm^{-2}.

Thus, we have evidence that ablating a solid target with ultrashort laser pulses several different thermodynamic paths in the temperature–density phase diagram of the irradiated material are followed, depending on the maximum attained temperature. The initial conditions experienced by the target uniquely determine the nature of the constituents of the ablation plasma and their relative abundances. Simulations indicate the ablation mechanisms and their dependence on the laser fluence, offering a picture of the process in qualitative agreement with experiments.

In conclusion, ultrashort laser pulses offer an efficient and clean way to synthesize NPs *in vacuum*. Although most of the systematic investigations were devoted to elemental systems, the basic mechanisms of laser–matter interaction have been identified, although their relative relevance to ablation is still under debate.

7.4 Applications

Lasers have been widely utilized in metallic materials machining since the early 1970s as well as in machining nonmetallic materials such as ceramics, plastics, various composites, and semiconductors (e.g., silicon, silicon carbide, etc.) for a number of industrial applications. The ability of lasers, especially pulsed lasers, to precisely machine micron and submicron features in otherwise difficult to machine materials such as ceramics and semiconductors has stimulated a rapidly growing interest in understanding the parameters controlling the limits and the capabilities of this process. Micromachining by laser ablation has become an alternative to other traditional micromachining methods such as photolithography. One reason is the recent developments in laser micromachining that have improved the ability to achieve well-defined 3-D structures at the micrometer scale. Situations suitable for laser micromachining are, for example, when the substrate material cannot be removed by etching (wet or dry) or when the substrate geometry is a complex one.

A large number of studies have been devoted to investigate laser-based micromachining that covered the different aspects of the machining process and the physics of laser–material interaction. The development of femtosecond (fs) lasers and their initial application to the machining of a variety of materials has created strong interest in their micromachining potential.

Current reasoning (see Sect. 7.3) suggests that the pulse duration of a femtosecond laser is so short that there is not sufficient time for any of the pulse energy to be distributed to the substrate in the form of heat. Thus, particularly for low pulse energies, there should be no heat-affected zone (HAZ) resulting from the processing.

This is in direct contrast to nanosecond (ns) machining, which has an associated HAZ. The magnitude of the HAZ is a direct result of the machining parameters and can be minimized for nanosecond micromachining. However, the HAZ is only one aspect of how a material is altered during the machining process. It is important also

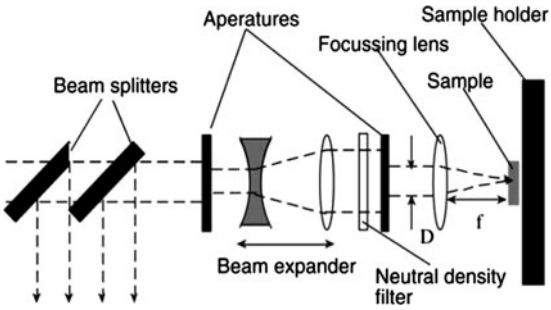

Fig. 7.7 Optical set-up for the laser machining [75]

to look at the stresses induced as a function of laser parameters. The optical set-up is simple (Fig. 7.7), involving a beam expander system (only if an ns laser is used).

We will briefly review some possible applications of laser processing. Lasers can be used for microdrilling, fine cutting, etching, thin films deposition, reshaping, etc. The pulsed lasers reported for being used for micronanomachining are working in nanosecond and femtosecond regimes. For the nanosecond lasers, there have been studies with excimer lasers, Nd:YAG, CO_2 [76–78]. There is an increased interest in using femtosecond lasers in micromachining, because of the high energy densities that can be obtained [79].

7.4.1 Direct Writing

Brodoceanu et al. [80] report on laser-induced patterning performed by "direct writing" (see Chap. 8 for a detailed description), where the laser light is just focused onto the substrate, by projection of the laser light through a mask, by direct-contact mask, or by the interference of laser beams. Nanoholes on Si(100) wafers were fabricated by using femtosecond Ti:sapphire laser radiation. A monolayer of amorphous silica microspheres of 150 nm radius is directly deposited onto the Si wafer by using a commercially available colloidal suspension. Figure 7.8 is an AFM image of the patterned Si substrate. A single pulse of 300 fs was used, at 266 nm. The fluence was $15 \pm 3.5\,\mathrm{m\,J\,cm^{-2}}$. The microspheres have a hexagonal lattice structure, and the distance between the holes represents the diameter of the spheres. The diameter at FWHM (full with at half maximum) is around 60 nm and the depth 6 nm, approximately.

7.4.2 Laser LIGA

An indirect way to use laser for microstructuring is called Laser-LIGA. This is a replication technique. It is a relatively low cost alternative to classic LIGA (using sichrotron radiation), if it is used in parallel mode. Laser LIGA makes use of the

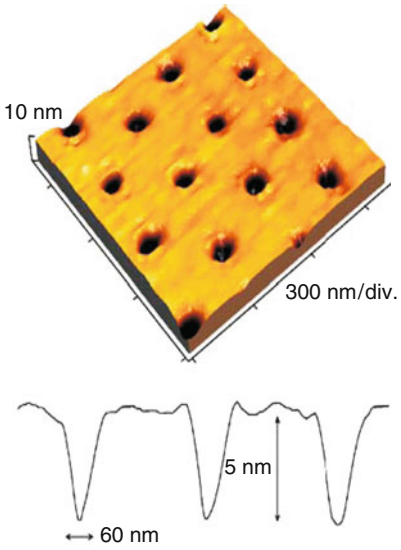

Fig. 7.8 Nanoholes fabricated on silicon by a single shot [80]

ablation of polymers (usually PMMA) followed by metallization (often with Ni or Cu). The typical processes are presented in [81] by Arnold et al. (Fig. 7.9). The main advantage of using Laser-LIGA is the fact that almost any geometry can be obtained and there is no need of masks, in most cases. The disadvantage is the fact that surface quality is better for X-ray lithography, and the maximum aspect ratios (up to 10) are considerably lower.

7.4.3 Laser Etching

Laser-assisted chemical etching is a method used for producing 3D structures *into substrates*. The laser light is used to activate a photochemical reaction. On the one hand, the laser activates the material, and on the other hand, it excites the etchant. The experiments can take place at atmospheric pressure.

Kazuyuki Minami et al. in [82] used a continuous wave Nd:YAG laser with a Q-switch unit for laser-assisted etching (LAE) of silicon. The laser worked in continuous mode because Q-switched created particles around the etched area. As etching gases, HCl, SF_6, NF_3, and CF_4 were investigated. The authors noticed that the p^+-Si can be heated and etched faster than the n-Si substrate. When the etching took place in the presence of HCl and in NF_3, there was no particle formation or redeposition. Al structures were etched in HCl, but they were not in NF_3.

Armacost et al. [83] used excimer laser at 193 nm to etch polysilicon in CF_3Br, CF_2Cl_2, and NF_3 atmosphere. There was almost no etching with CF_2Cl_2, some etching with CF_3Br, and smooth profiles were obtained with NF_3.

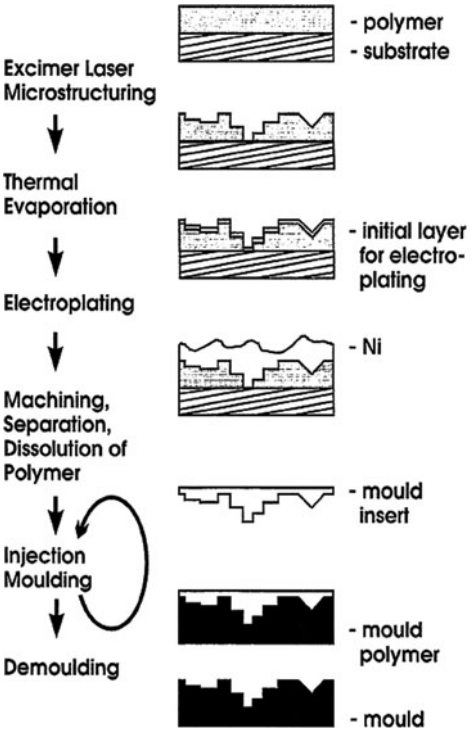

Fig. 7.9 Laser-LIGA processes [81]

Barada K. Nayak in [84] reported the etching of silicon and germanium after irradiating with femtosecond laser in sulfur hexafluoride (SF_6) and hydrogen chloride (HCl). Features with size in the nanometer range have been obtained. Figure 7.10 presents SEM images of structures formed in silicon surface by 240 laser pulses of 130 fs duration, at 0.6 J cm^{-2} in 40 kPa of (a) SF_6 and (b) HCl.

7.4.4 Pulsed Laser Deposition

Pulsed laser deposition (PLD) is particularly interesting due to its versatility in the deposition of materials, even with a complex stoichiometry [4]. PLD in vacuum permits to produce films assembled atom by atom, achieving even epitaxial growth in particular conditions (e.g., with heated substrates).

In the presence of a suitable background gas pressure, laser ablation may result in cluster formation during plume expansion. In the synthesis of nanostructured thin films, the characterization of the growth processes plays a fundamental role for the control of the film and surface properties. In particular, when the deposition technique is based on the production and assembling of nanoparticles-clusters, the

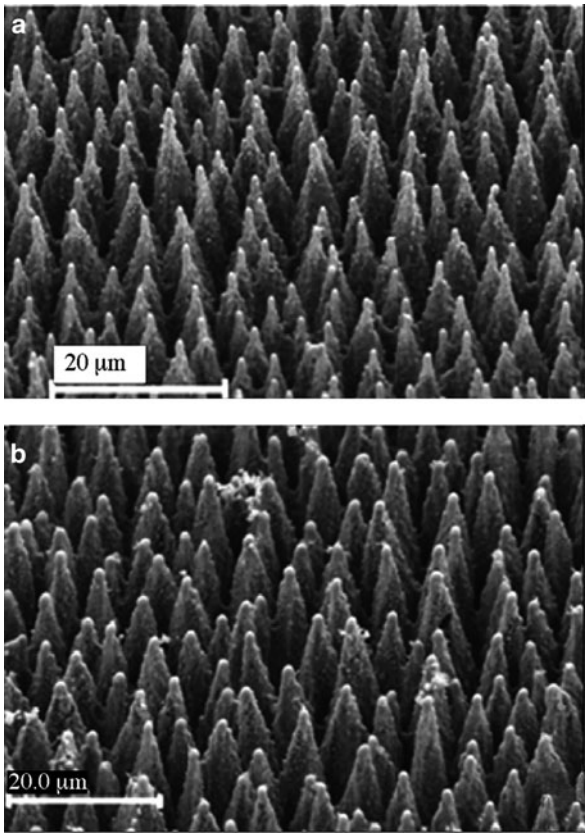

Fig. 7.10 SEM images of structures, formed in a silicon surface by 240 laser pulses of 130 fs duration, at 0.6 J cm^{-2} in 40 Pa of (**a**) SF_6 and (**b**) HCl [84]

characterization of the precursor size distribution as well as of the first stages of film formation is of fundamental importance (see Sects. 7.2.2 and 7.3).

Factors influencing the laser ablation process include the laser beam parameters, such as wavelength, energy, or fluence, and pulse length, the material properties of the target, such as melting temperature, thermal diffusion rate, optical reflectivity, and the ambient, whether a gas, or a liquid. By the correct combination of these parameters, it is possible to implement surface features with a complex 3-D geometry on virtually any material surface, and by choosing a specific micromachining environment, for example, vacuum, gas, or liquid with appropriate composition, it is possible to control the laser-induced chemical changes of the material surface.

A typical PLD set-up is described in Fig. 7.11. This consists basically of four components: a laser, a reaction chamber, a target, and a substrate. When the deposition takes place in chemically reactive gas, the ablated substance reacts with the gas molecules, and the film can differ completely from the starting material. This

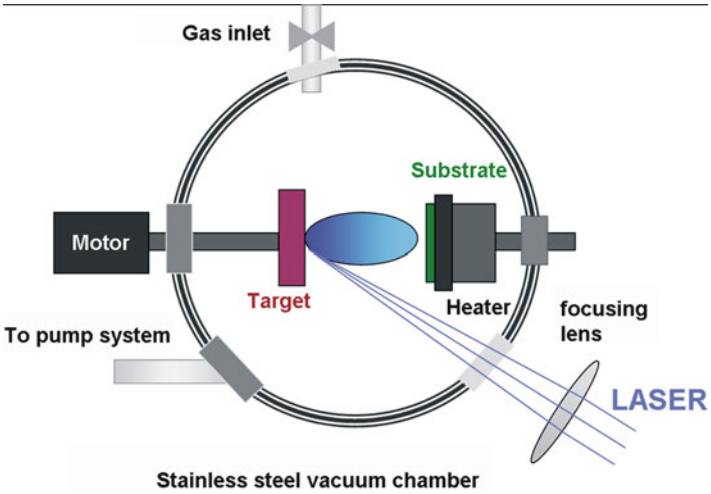

Fig. 7.11 Standard PLD set-up

method is called reactive pulsed laser deposition and is sustained by the fact that the ablated species are highly reactive and have energies between 1 and 20 eV.

Uniform ablation of the target is obtained through its rotation and translation with respect to the laser radiation. The distance between the target and substrate is generally of a few centimeters. The film uniformity can be improved if the substrate is moved with respect to the plasma direction, for example, rotating eccentrically the substrate holder.

The substrate temperature is a very important parameter for the morphology, microstructure, and crystallinity of the deposited films. For a good control of the temperature, thermocouples are placed under the substrate.

Nanoparticles play an important role in a wide variety of fields including advanced materials, biomedical field (sensors for disease detection (quantum dots), programmed release drug delivery systems), and environmental (clean up of soil contamination and pollution, biodegradable polymers, treatment of industrial emissions), electronics, pharmaceuticals, etc. Embedding nanoparticles in a matrix, complex compounds with tailored characteristics can be obtained. Combining polymers with different properties (for example optical, or electrical properties) with clusters of metals, new materials can be obtained, with new macroscopic characteristics. This class of compounds where metallic nanoclusters are embedded in polymeric matrices is suitable for packaging applications.

An interesting work on this topic has been carried out by Röder et al. in 2008 [85]. They report on the use of PLD to grow nanostructured materials formed by *metallic clusters* (Ag, Au, Pd, and Cu) and *polymeric matrices* (polycarbonate – PC and poly (methyl methacrylate) – PMMA). The metal clusters embedded in PC were grown using a KrF excimer laser with pulse duration of 30 ns, working at 248 nm, and repetition rate of 10 Hz. The work has been performed at room

temperature in UHV deposition chamber with the base pressure of 10^{-6} Pa. As reported in [85], smooth polycarbonate thin films of about 20 nm were deposited at a fluence of 70 mJ cm^{-2}. On these films, the metals were deposited at fluences in the range of 4–6 J cm^{-2} and they had an average thickness of less than 5 nm. Two processes take place during metal ablation in vacuum: deposition of metal on the polymeric surface and ion implantation some nanometers below the surface. The nanocluster dimension and shape depend both on the metal and on the polymer type. TEM investigations evidence that the nanocluster are formed inside the polymer, just below its surface, by the ion diffusion processes followed by the Volmer–Weber island formation. As it can be seen from the pictures in Figs. 7.12 and 7.13 [85], the clusters grow separately. When the number of pulses increases, fewer islands are formed, with bigger size, due to coalescence processes. The clusters are, in general, spherical, but a tendency to different shapes can be noticed, depending on the metal and/or on the polymer. J. Röder et al. concluded that the Ag clusters show larger distances on PMMA, because of a higher diffusivity of Ag on PMMA than on PC. Pd and Cu exhibit a high reactivity with the polymer. This decreases the diffusion and results in a bigger number of clusters of smaller sizes.

Tungsten oxide is a chromogenic compound with various applications in gas sensing (it detects both H_2S and H_2, and small concentrations of NO and Cl_2) [86, 87]. The sensing efficiency depends also on the surface morphology of the

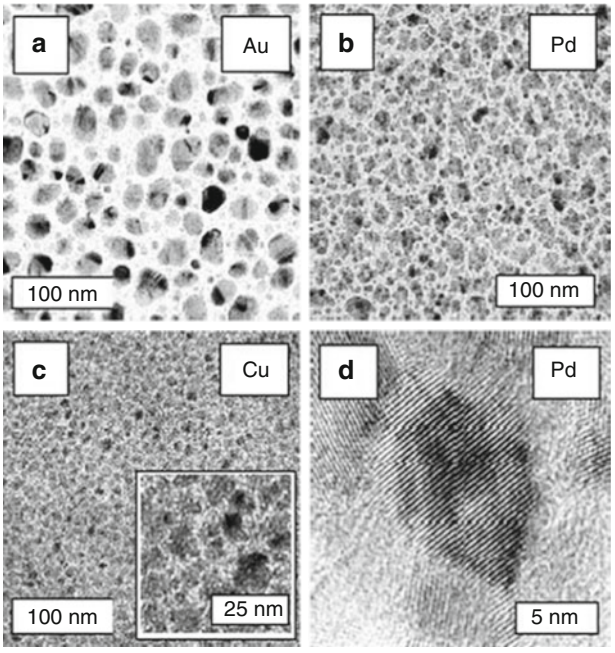

Fig. 7.12 TEM images of different metals between two 20-nm-thick PC layers with average metal amounts of (**a**) 7.3 nm for Au, (**b**) 3.3 nm for Pd, (**c**) 3.8 nm for Cu, and (**d**) 3.3 nm for Pd [85]

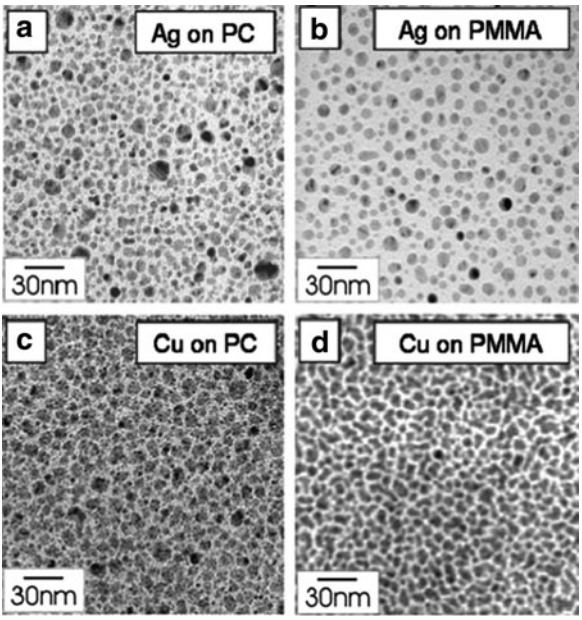

Fig. 7.13 TEM images of Ag and Cu clusters grown between two 20-nm-thick PC layers and on 15-nm PMMA, respectively, with metal amounts of (**a**) 1.9 nm for Ag on PC, (**b**) 2.0 nm for Ag on PMMA, (**c**) 3.8 nm for Cu on PC, and (**d**) 3.6 nm for Cu on PMMA [85]

active material. In particular a high-specific area value A_s is desirable. Cluster-assembled (CA) films are suitable to get high A_s values however, it is often difficult to deposit CA films in a reproducible way with an acceptable mechanical stability and adhesion to the substrate.

Filipescu et al. in [88] reported the growth of WO_x by laser ablation using a W target at room temperature in oxygen reactive pressure. A Nd:YAG laser with 4 harmonics was used, and a radiofrequency (RF) discharge system was added to increase the reactivity. The information regarding the WO_x film morphology was supplied by SEM observations.

The microstructure of some WO_x samples that were synthesized in the presence of a radio-frequency consists of a dense nanostructure made of irregularly shaped agglomerates (Fig. 7.14) whose typical size lowers with increasing O_2 pressure, from about 80 nm (sample deposited at 300 Pa) to 40 nm (sample deposited at 500 Pa) to 20 nm (samples deposited at 700 and 900 Pa). The addition of RF is efficient to induce film nanostructuring, resulting in an open microstructure much more prone to oxidation, also after the deposition is completed, than the compact films produced without RF power. Consequently, at fixed substrate temperature, the cluster ability to migrate and reciprocally aggregate giving bigger agglomerates is progressively reduced with increasing buffer gas pressure.

PLD technique can be also used for the *growth of nanowires* as presented by N. Wang et al. in [89], which is a very interesting review about the growth of

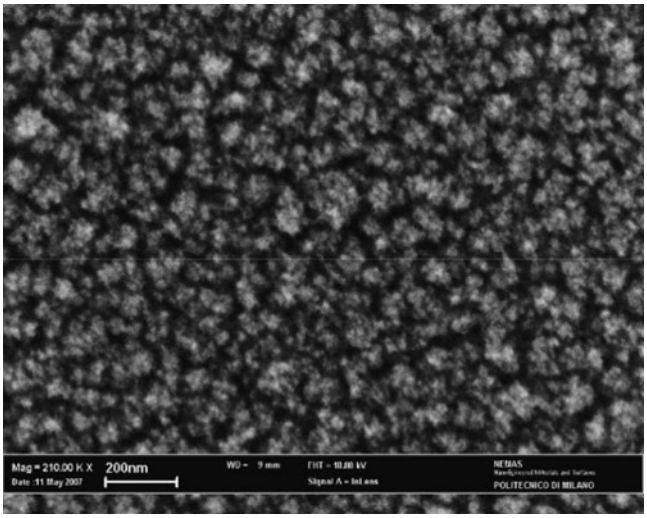

Fig. 7.14 Representative surface microstructure of a WO_x film deposited with the assistance of RF power (100 W) [88]

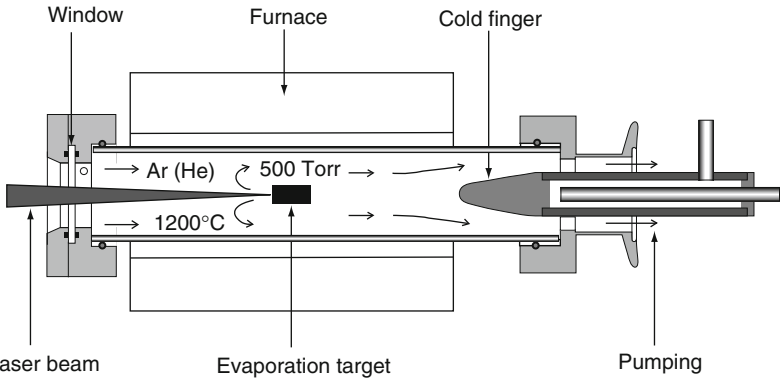

Fig. 7.15 Experimental setup for the synthesis of Si nanowires by laser ablation (Prof. I. Bello) [89]

nanowires. A schematic of a laser ablation experimental setup that can be used to grow nanowires is shown in Fig. 7.15.

Any kind of high-power pulsed laser can be used: Nd:YAG, excimer laser, femto-second lasers. For example, in [90], A.M. Morales and C.M. Lieber reported laser ablation cluster formation and vapor–liquid–solid (VLS) growth for crystalline semiconductor nanowires synthesis. Silicon and germanium nanowires with diameters of 6–3 and 3–9 nm, respectively, and lengths between 1 and 30 microns (for Si) have been obtained using a Nd:YAG laser working at 532 nm to ablate targets containing the element of the nanowire and the metal catalyst as well. Figure 7.16

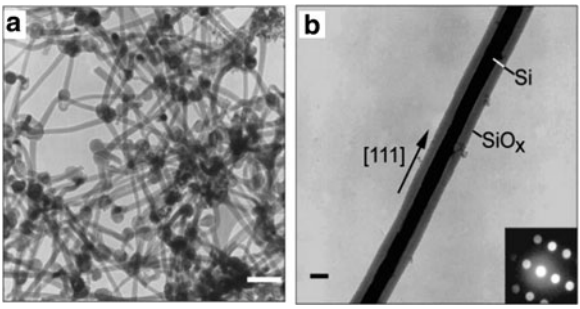

Fig. 7.16 (**a**) TEM image of the nanowires produced after ablation of a $Si_{0.9}Fe_{0.1}$ target. The scale on is 100 nm. The temperature was 1,473 K and the pressure ∼66 kPa Ar flowing at 50 SCCM. (**b**) Diffraction contrast TEM image of a Si nanowire. The scale represents 10 nm [90]

presents high resolution TEM images of individual Si nanowires. The nanowire has a uniform crystalline core covered by an amorphous coating.

7.4.5 Matrix-Assisted Pulsed Laser Evaporation (MAPLE)

The MAPLE technique used for the deposition of carbon nanostructures is described in [91]. Hunter et al. report on the deposition of carbon nanopearls (also known as nanospheres) by MAPLE and also the use of the process simultaneously with magnetron sputtering to encapsulate nanopearls within a gold film. They investigated the effects of: (a) solvent material; (b) laser repetition rate; (c) laser pulse energy; (d) substrate temperature; and (e) background pressure.

In Fig. 7.17, the carbon nanopearls, which were successfully embedded within the gold layer of approximately 1 μm in thickness can be seen. The aim of the study was to find the optimal parameters for depositing disperse, droplet-free films of carbon nanopearls with a large field of applications such as tribological coatings. These parameters were found to be toluene matrix, 700 mJ, 1 Hz, 373 K substrate temperature, and unregulated vacuum pressure or 2.67 Pa in argon.

MAPLE technique has also been successfully used for the deposition of nanostructured titania (TiO_2) nanoparticles thin films to be used for gas sensing applications as it was reported in [92]. Caricato et al. reported on the deposition of an uniform distribution of TiO_2 nanoparticles with an average size of about 10 nm on Si and interdigitated Al_2O_3 substrates (Fig. 7.18). To investigate the thin films, they used high-resolution scanning electron microscopy-field emission gun (SEM-FEG). Energy dispersive X-ray (EDX) analysis revealed the presence of only the titanium and oxygen signals and by FTIR (Fourier transform infrared) spectroscopy, the TiO_2 characteristic composition and bond were revealed.

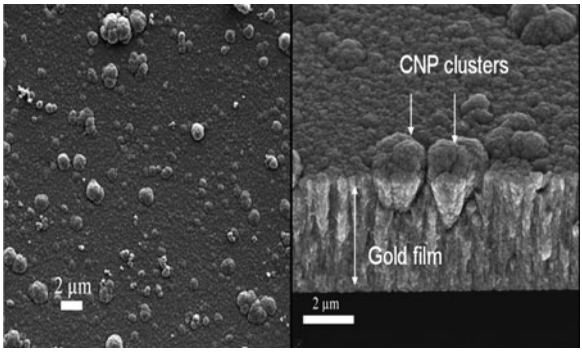

Fig. 7.17 Carbon nanopearls embedded in a gold coating synthesized using MAPLE and magnetron sputtering: *left* – top view; *right* – cross section [91]

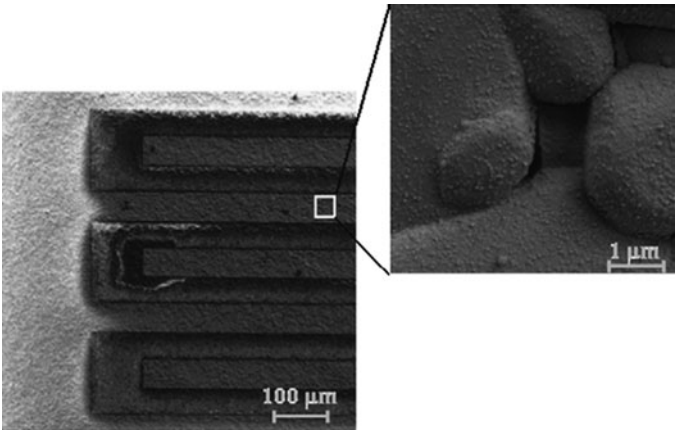

Fig. 7.18 Scanning electron microscopy images of the interdigitated sensor and of the TiO_2 film morphology on the Al_2O_3 grains [92]

7.4.6 Laser-Assisted Chemical Vapor Deposition (LA-CVD)

Single-walled nanotubes are a very important variety of carbon nanotube because they exhibit important mechanical and electrical properties and also offer great promise as active elements in the "nano-electromechanical" systems. They have a wide range of applications as high-frequency oscillators and filters, nanoscale wires, transistors and sensors.

In [93], Liu et al. reported on the nucleation and rapid growth of single-wall carbon nanotubes (SWNTs) by pulsed-laser-assisted chemical vapor deposition (PLA-CVD). The deposition system is shown in Fig. 7.19. A special high-power, Nd:YAG laser system with tunable pulse width (>0.5 ms) was used to rapidly heat ($> 3\times10^4\ \mathrm{K\,s^{-1}}$) metal catalyst-covered substrates to different growth temperatures

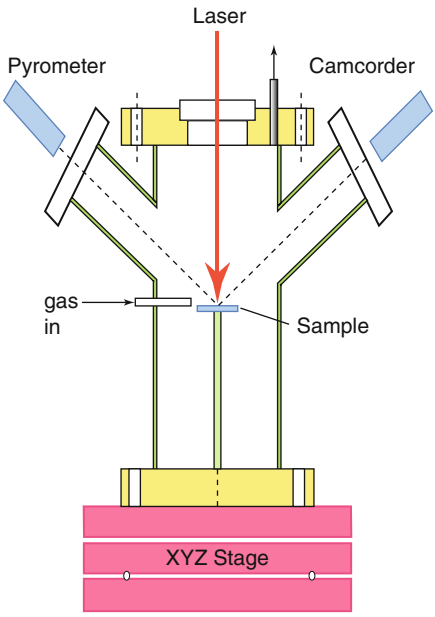

Fig. 7.19 Schematic of a PLA-CVD chamber [93]

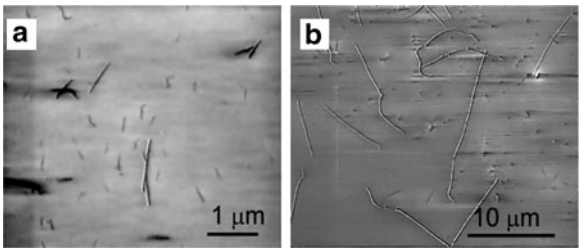

Fig. 7.20 SEM images of nanotubes grown from a single 50 ms laser pulse (52 J) using (**a**)/(**b**) Fe/Al_2O_3 thin film and ferritin as catalysts, respectively [93]

for very brief (subsecond) and controlled time intervals. SWNTs were found to grow under rapid heating conditions, with a minimum nucleation time of >0.1 s. The growth rates by single laser pulse were found to be up to 100 $\mu m\, s^{-1}$. SEM images of nanotubes obtained using thin film catalysts (a) and ferritin nanoparticles (b) are shown in Fig. 7.20.

Another example concerning the synthesis of SWNTs and SWNHs (single-walled nanohorns) is given in [94], exploring the continuous ablation regime for the growth of SWCN and the cumulative ablation regime, which is optimal for the growth of SWNTs with catalyst assistance. An industrial Nd:YAG laser (600 W, 1–500 Hz repetition rate) with tunable pulse widths (0.5–50 ms) was used. Carbon is shown to self-assemble into single-wall nanohorn structures at rates of ~1 $nm{\cdot}ms^{-1}$, which is comparable to the catalyst-assisted SWNT growth rates measured in [95]. Figure 7.21 shows TEM images of SWNHs synthesized at the optimized conditions

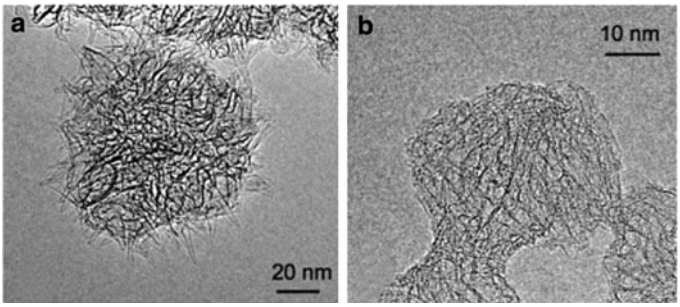

Fig. 7.21 TEM images of SWNHs synthesized using (**a**) 20 ms, 5 Hz repetition rate, and (**b**) 0.5 ms, 80 Hz laser pulses [94]

using 20 ms laser pulses at a low laser pulse repetition rate of 5 Hz and 0.5 ms pulses at 80 Hz.

7.4.7 Lasers for MEMS (Micro-Electro-Mechanical Systems)

MEMS fabrication and semiconductor industry is a very large area, searching for new technologies to assure high quality, speed, and reliability. The field of micro-electro-mechanical systems is still dominated by the silicon technology. There are also other good candidates to replace silicon as wafers like gallium arsenide, germanium, gallium phosphide, indium phosphide, sapphire, quartz etc. The laser is a very good tool for the micronanoprocessing of these materials, and also other types of materials such as metals, ceramics, and polymers can be processed.

Figure 7.22 is an example and presents a MEMS built by Sandia National Laboratories [96]. Some of the advantages of using lasers in MEMS fabrications are listed in the following:

- Reliability
- Speed
- Relatively low cost
- Selectivity (based on the fine focusing that can be achieved)

7.5 Concluding Remarks

Lasers have been demonstrated to be a clean and efficient tool to produce and/or to assist obtaining nanostructures of different materials, from simple metals to complex nanocomposites. The size, form, distribution, and density of nanostructures depend both on experimental parameters (laser wavelength, fluence and pulse duration, substrate type, and temperature) and on target material. Particles and/or nanostructures with tailored properties can be obtained by a careful control of process parameters.

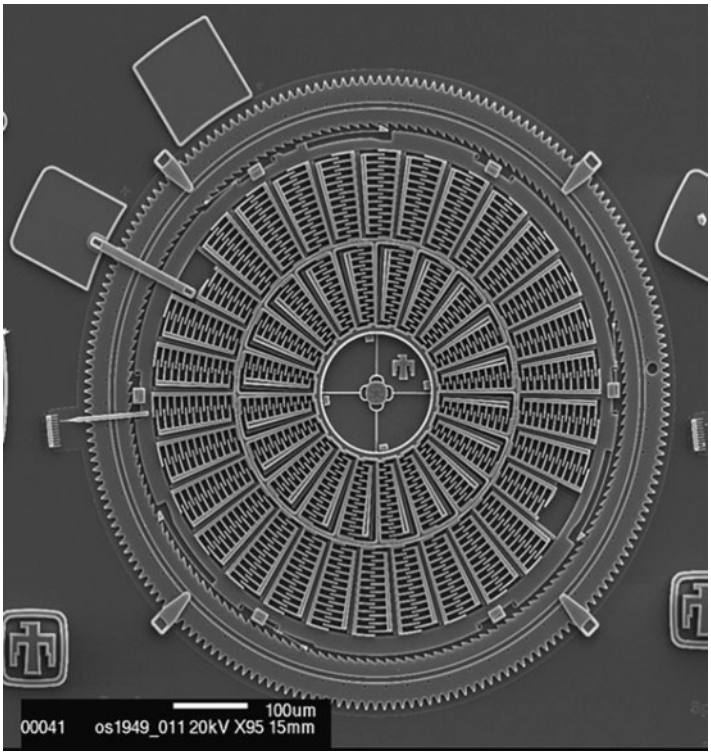

Fig. 7.22 The Torsional Ratcheting Actuator (TRA). The TRA uses a rotationally vibrating (oscillating) inner frame to ratchet its surrounding ring gear. Charging and discharging the inner interdigitated comb fingers causes this vibration (Sandia National Laboratories) [96]

NP synthesis by ns laser ablation in an ambient gas is a bottom-up strategy that is approaching the stage of designing experimental conditions to deposit on a suitable substrate arrays of dispersed NPs with predefined size and composition. Such a condition is essential to finely tune the physico-chemical properties of the NPs and those of the resulting nanostructure. Energy exchanges occurring both in the plasma and between plasma and ambient gas during plume propagation affect NP growth, besides determining the energy available to particle interaction on the substrate. Plasma interaction with ambient atmosphere is a complex gas dynamic phenomenon including scattering, slowing down, thermalization, diffusion, and recombination of the ablated particles, formation of shock waves, and particle clustering. By modeling plasma propagation, the average size of NPs grown in the plume up to their steady size can be calculated.

Ultrashort laser pulses have shown to be a conceptually simple and clean way to synthesize NPs in vacuum; the basic mechanisms of laser–matter interaction have been identified. Attention was mainly focussed onto the dependence of the different ablation mechanisms on laser fluence, yet ablation is sensitive to target

morphology, including crater formation, to the uniformity of energy distribution of the laser spot, to the size of the latter. Besides this, elemental targets were mostly investigated. Chemical effects, both concerning compound targets and interactions between plasma constituents and residual reactive gases were nearly neglected. Such topics need further investigation before fs laser ablation can be considered a reliable bottom-up strategy to prepare NP assemblies and CA films with ad-hoc designed properties.

References

1. D.B. Geohegan, A.A. Puretzky, G. Duscher, S.J. Pennycook, Appl. Phys. Lett. **72**, 2987 (1998)
2. D. Scuderi, O. Albert, D. Moreau, P.P. Pronko, J. Etchepare, Appl. Phys. Lett. **86**, 071502 (2005)
3. B. Holian, D. Grady, Phys. Rev. Lett. **60**, 1355 (1988)
4. T. Yoshida, S. Takeyama, Y. Yamada, K. Mutoh, Appl. Phys. Lett. **68**, 1772 (1996)
5. S. Eliezer, N. Eliaz, E. Grossman, D. Fisher, I. Gouzman, Z. Henis, S. Pecker, Y. Horovitz, S. Fraenckel, M. Maman, Y. Lereah, Phys. Rev. B **69**, 144119 (2004)
6. S. Amoruso, J. Schou, J.G. Lunney, Appl. Phys. A Mater. Sci. Process. **92**, 907 (2008)
7. O. Albert, S. Roger, Y. Glinec, J.C. Loulergue, J. Etchepare, C. Boulmer-Leborgne, J. Perrière, E. Million, Appl. Phys. A Mater. Sci. Process. **76**, 319 (2003)
8. X.T. Wang, B.Y. Man, G.T. Wang, Z. Zhao, B.Z. Xu, Y.Y. Zia, L.M. Mei, X.Y. Hu, J. Appl. Phys. **80**, 1783 (1996)
9. Z. Zhang, P.A. VanRompay, J.A. Nees, P.P. Pronko, J. Appl. Phys. **92**, 2867 (2002)
10. S. Noël, J. Hermann, T. Itina, Appl. Surf. Sci. **253**, 6310 (2007)
11. S.I. Anisimov, D. Bäuerle, B.S. Luk'yanchuk, Phys. Rev. B **48**, 12076 (1993)
12. Y.B. Zel'dowich, Y.P. Raizer, *Physics of Shock Waves and High-temperature Hydrodynamic Phenomena* (Academic, New York, 1966)
13. S. Amoruso, A. Sambri, X. Wang, J. Appl. Phys. **100**, 013302 (2006)
14. A.K. Sharma, R.K. Thareja, Appl. Surf. Sci. **243**, 68 (2005)
15. T.E. Itina, J. Hermann, P. Delaporte, M. Sentis, Phys. Rev. E **66**, 066406 (2002)
16. R.F. Wood, J.N. Leboeuf, D.B. Geohegan, A.A. Puretzky, K.R. Chen, Phys. Rev. B **58**, 1533 (1998)
17. G.W. Martin, L.A. Doyle, A.A. Khateeb, I. Weaver, D. Riley, M.J. Lamb, T. Morrow, C.L.S. Lewis, Appl. Surf. Sci. **127–129**, 710 (1998)
18. S.S. Harilal, C.V. Bindhu, M.S. Tillack, F. Najmabadi, A.C. Gaeris, J. Appl. Phys. **93**, 2380 (2003)
19. D.B. Geohegan, Appl. Phys. Lett. **60**, 2732 (1992)
20. J. Gonzalo, C.N. Afonso, I. Madariaga, J. Appl. Phys. **81**, 951 (1997)
21. A.V. Rode, E.G. Gamaly, B. Luther-Davies, Appl. Phys. A Mater. Sci. Process. **70**, 135 (2000)
22. P.M. Ossi, in *Laser-surface interactions for new materials production: Tailoring structure and properties*, ed. by A. Miotello, P.M. Ossi (Springer, Berlin, 2009), p. 99
23. R.F. Wood, K.N. Chen, J.N. Leboeuf, A.A. Puretzky, D.B. Geohegan, Phys. Rev. Lett. **79**, 1571 (1997)
24. V. Gusarov, I. Smurov, J. Phys. D Appl. Phys. **36**, 2962 (2003)
25. M.S. Tillack, D.W. Blair, S.S. Harilal, Nanotechnol. **15**, 390 (2004)
26. A. Peterlongo, A. Miotello, R. Kelly, Phys. Rev. E **50**, 4716 (1994)
27. A. Bailini, P.M. Ossi, Appl. Surf. Sci. **252**, 4364 (2006)
28. S. Acquaviva, M.L. De Giorgi, Appl. Surf. Sci. **186**, 329 (2002)
29. A. Quarteroni, *Modellistica Numerica per Problemi Differenziali* (Springer, Milano, 2003), p. 105

30. D. Bolgiaghi, A. Miotello, P. Mosaner, P.M. Ossi, G. Radnoczi, Carbon **43**, 2122 (2005)
31. A. Bailini, P.M. Ossi, A. Rivolta, Appl. Surf. Sci. **253**, 7682 (2007)
32. A. Bailini, P.M. Ossi, Europhys. Lett. **79**, 35002 (2007)
33. P.M. Ossi, A. Bailini, Appl. Phys. A Mater. Sci. Process. **93**, 645 (2008)
34. E. Fazio, F. Neri, P.M. Ossi, N. Santo, S. Trusso, Laser Part. Beams **27**, 281 (2009)
35. M.F. Zhou, Z.W. Fu, Q.Z. Qin, Appl. Surf. Sci. **125**, 208 (1998)
36. J.C. Orlianges, C. Champeaux, A. Catherinot, T. Merle, B. Angleraud, Thin Solid Films **453–454**, 285 (2004)
37. Y. Yamagata, A. Sharma, J. Narayan, R.M. Mayo, J.W. Newman, K. Ebihara, J. Appl. Phys. **88**, 6861 (2000)
38. C. Vivien, J. Hermann, A. Perrone, C. Boulmer-Leborgne, A. Luches, J. Phys. D Appl. Phys. **31**, 1263 (1998)
39. P. Jensen, Rev. Mod. Phys. **71**, 1695 (1999)
40. E. Irissou, B.L. Drogoff, M. Chaker, D. Guay, J. Appl. Phys. **94**, 4796 (2003)
41. R. Dolbec, E. Irissou, M. Chaker, D. Guay, F. Rosei, M.A.E. Khakani, Phys. Rev. B **70**, 201406 (2005)
42. C.N. Afonso, J. Gonzalo, R. Serna, J.C.G. de Sande, C. Ricolleau, C. Grigis, M. Gandais, D.E. Hole, P.D. Townsend, Appl. Phys. A Mater. Sci. Process. **69**, 201 (1999)
43. P.O. Jubert, O. Fruchart, C. Meyer, Surf. Sci. **522**, 8 (2003)
44. P. Ohresser, J. Shen, J. Barthel, M. Zheng, C.V. Mohan, M. Klaua, J. Kirschner, Phys. Rev. B **59**, 3696 (1999)
45. J. Gonzalo, A. Perea, D. Babonneau, C.N. Afonso, N. Beer, J.P. Barnes, A.K. Petford-Long, D.E. Hole, P.D. Townsend, Phys. Rev. B **71**, 125420 (2005)
46. W. Marine, L. Patrone, B. Luk'yanchuk, M. Sentis, Appl. Surf. Sci. **154–155**, 345 (2000)
47. A. Bailini, P.M. Ossi, Carbon **44**, 3049 (2006)
48. F. Di Fonzo, A. Bailini, V. Russo, A. Baserga, D. Cattaneo, M.G. Beghi, P.M. Ossi, C.S. Casari, A.Li. Bassi, C.E. Bottani, Catal. Today **116**, 69 (2006)
49. P.M. Ossi, A. Bailini, O. Geszti, G. Radnoczi, Europhys. Lett. **83**, 68005 (2008)
50. B. Fazio, S. Trusso, E. Fazio, F. Neri, P.M. Ossi, N. Santo, Rad. Eff. Def. Sol. **163**, 673 (2008)
51. R.W. Siegel, in *Physics of New Materials*, ed. by F.E. Fujita (Springer, Berlin, 1998), p. 66
52. D.B. Geohegan, A.A. Puretzky, Appl. Surf. Sci. **96–98**, 131 (1996)
53. D.H. Lowndes, C.M. Rouleau, T. Thundat, G. Duscher, E.A. Kenik, S.J. Pennycook, Appl. Surf. Sci. **127–129**, 355 (1998)
54. E. Fazio, F. Neri, P.M. Ossi, N. Santo, S. Trusso, Appl. Surf. Sci. **255**, 9676 (2009)
55. W.S. Rasband, ImageJ, *http://rsb.info.nih.gov/ij/* (1997–2005)
56. C.R. Henry, Surf. Sci. Rep. **31**, 231 (1998)
57. P. Mulvaney, Langmuir **12**, 788 (1996)
58. Y. Sun, Y. Xia, Science **298**, 2176 (2002)
59. R. Jin, Y.W. Cao, C.A. Mirkin, K.L. Kelly, G.C. Shatz, J.G. Zheng, Science **294**, 1901 (2001)
60. Y. Okano, K. Oguri, T. Nishikawa, H. Nakano, Appl. Phys. Lett. **89**, 221502 (2006)
61. S. Amoruso, G. Ausanio, A.C. Barone, R. Bruzzese, C. Campana, X. Wang, Appl. Surf. Sci. **254**, 1012 (2007)
62. C. Boulmer-Leborgne, B. Benzerga, J. Perrière, Proc. SPIE **6261**, 20 (2006)
63. J.V. Rau, A. Latini, A. Generosi, V.R. Albertini, D. Ferro, R. Teghil, S.M. Barinov, Acta Mater. **57**, 673 (2009)
64. C. Boulmer-Leborgne, in *Laser-surface interactions for new materials production: Tailoring structure and properties*, ed. by A. Miotello, P.M. Ossi (Springer, Berlin, 2009), p. 125
65. L.V. Zhigilei, Appl. Phys. A Mater. Sci. Process. **76**, 339 (2003)
66. K. Eidmann, J.M. ter Vehn, T. Schlegel, S. Hüller, Phys. Rev. E **62**, 1202 (2000)
67. T.E. Glover, J. Opt. Soc. Am. B **20**, 125 (2003)
68. B.J. Garrison, T.E. Itina, L.V. Zhigilei, Phys. Rev. E **68**, 041501 (2003)
69. A. Cavalleri, K. Sokolowski-Tinten, J. Bialkowski, M. Schreiner, D. von der Linde, J. Appl. Phys. **85**, 3301 (1999)
70. M.Q. Ye, C.P. Grigoropoulos, J. Appl. Phys. **89**, 5183 (2001)
71. D. Grojo, J. Hermann, A. Perrone, J. Appl. Phys. **97**, 063306 (2005)

72. T.E. Itina, K. Gouriet, L.V. Zhigilei, S. Noël, J. Hermann, M. Sentis, Appl. Surf. Sci. **253**, 7656 (2007)
73. M.E. Povarnitsyn, T.E. Itina, M. Sentis, K.V. Khishchenko, P.R. Levashov, Phys. Rev. B **75**, 235414 (2007)
74. H. Haberland, in *Clusters of Atoms and Molecules*, ed. by H. Haberland (Springer, Berlin, 1994), p. 205
75. H. Huang, H.Y. Zheng, G.C. Lim, Appl. Surf. Sci. **228**, 201 (2004)
76. C. Molpeceres, S. Lauzurica, J.J. García-Ballesteros, M. Morales, J.L. Ocaña, Microel. Eng. **84**, 1337 (2007)
77. M. Goller, N. Lutz, M. Geiger, J. Eur. Ceram. Soc. **12**, 315 (1993)
78. N.C. Nayak, Y.C. Lam, C.Y. Yue, A.T. Sinha, J. Micromech. and Microeng. **18**, 095020 (2008)
79. A.S. Holmes, Proc. SPIE, **4274**, 297 (2001)
80. D. Brodoceanu, L. Landström, D. Bäuerle, Appl. Phys. A Mater. Sci. Process. **86**, 313 (2007)
81. J. Arnold, U. Dasbach, W. Ehrfeld, K. Hesch, H. Löwe, Appl. Surf. Sci. **86**, 251 (1995)
82. K. Minami, Y. Wakabayashi, M. Yoshida, K. Watanabe, M. Seashi, J. Micromech. Microeng. **3**, 81 (1993)
83. M.D. Armacost, S.V. Babu, S.V. Nguyen, J.F. Rembetski, J. Mater. Res. **2**, 895 (1987)
84. B.K. Nayak, M.C. Gupta, K.W. Kolasinski, Appl. Surf. Sci. **253**, 6580 (2007)
85. J. Röder, J. Faupel, H.U. Krebs, Appl. Phys. A Mater. Sci. Process. **253**, 863 (2008)
86. P.V. Ashirt, G. Bader, V. Truong, Thin Solid Films **320**, 324 (1998)
87. Z. Xu, J.F. Vetelino, R. Lec, D.C. Parker, J. Vac. Sci. Technol. A **8**, 3634 (1990)
88. M. Filipescu, P.M. Ossi, M. Dinescu, Appl. Surf. Sci. **254**, 1347 (2007)
89. N. Wang, Y. Cai, R.Q. Zhang, Mat. Sci. Eng., R **60**, 1 (2008)
90. A.M. Morales, C.M. Lieber, Science **279**, 208 (1998)
91. C.N. Hunter, M.H. Check, J.E. Bultman, A.A. Voevodin, Surf. Coat. Tech. **203**, 300 (2008)
92. A.P. Caricato, S. Capone, G. Ciccarella, M. Martino, R. Rella, F. Romano, J. Spadavecchia, A. Taurino, T. Tunno, D. Valerini, Appl. Surf. Sci. **253**, 7937 (2007)
93. Z. Liu, D.J. Styers-Barnett, A.A. Puretzky, C.M. Rouleau, D. Yuan, I.N. Ivanov, K. Xiao, J. Liu, D.B. Geohegan, Appl. Phys. A Mater. Sci. Process. **93**, 987 (2008)
94. A.A. Puretzky, D.J. Styers-Barnett, C.M. Rouleau, H. Hu, B. Zhao, I.N. Ivanov, D.B. Geohegan, Appl. Phys. A Mater. Sci. Process. **93**, 849 (2008)
95. A.A. Puretzky, H. Schittenhelm, X. Fan, M.J. Lance, L.F. Allard Jr, D.B. Geohegan, Phys. Rev. B **65**, 245425 (2002)
96. *http://mems.sandia.gov/gallery/images_torsional_ratcheting_actuator.html*